UNIVERSITY OF CALIFORNIA SAN DIEGO

From Black to White: An Investigation of the Link between Marine Carbonate Geochemistry and Color Over the Past 500 Million Years

A Thesis submitted in partial satisfaction of the requirements
for the degree Master of Science

in

Earth Sciences

by

Robert Joseph

Committee in charge:

Professor Richard Norris, Chair
Professor Geoffrey Cook
Professor Jeffrey Gee

2023

The Thesis of Robert Joseph is approved, and it is acceptable in quality and form for publication on microfilm and electronically.

University of California San Diego

2023

DEDICATION

This thesis is dedicated to the late Professor Jane Teranes, without whom I would not have gotten this far.

And to Jay and Jennifer Joseph, whose support as parents was invaluable.

TABLE OF CONTENTS

LIST OF FIGURES

LIST OF TABLES

LIST OF ABBREVIATIONS

Ma	Million Years
Mya	Million Years Ago
BSR	Bacterial Sulfate Reduction
OM	Organic Matter
XRF	X-Ray Fluorescence
Wt%	Weight Percent
LOD	Lack of Data
%IncMSE	Percent Increase in Mean Standard Error
IncNodePurity	Increase in Node Purity
PCA	Principal Component Analysis
PC	Principal Component
RDA	Redundancy Analysis
EO	Element-only
ECT	Element-color-time
TOC	Total Organic Carbon
ICP	Inductively Coupled Plasma

LIST OF SUPPLEMENTAL FILES

joseph_random_forest_r_markdown.Rmd

joseph_figure_creation_r_markdown.Rmd

joseph_full_xrf_scans.xlsx

joseph_matched_reflectance_geochem_data.csv

joseph_ecrm_values.csv

joseph_ghnp_values.csv

joseph_sdar_h1_values.csv

joseph_sdar_l2_values.csv

ACKNOWLEDGEMENTS

The color, age, depositional environment, and location data used in this thesis were previously collected and arranged by Rishi K. Sugla and Professor Richard Norris.

VITA

2021 Bachelor of Science in Geosciences, University of California San Diego

2023 Master of Science in Earth Sciences, University of California San Diego

ABSTRACT OF THE THESIS

From Black to White: An Investigation of the Link between Marine Carbonate Geochemistry and Color Over the Past 500 Million Years

by

Robert Joseph

Master of Science in Earth Sciences

University of California San Diego, 2023

Professor Richard Norris, Chair

Marine carbonates display a marked color transition from dark gray in the early Paleozoic to predominantly white and tan in the Mesozoic. Previous studies have interpreted this transition to reflect a fundamental change in the redox state of marine sediments around ~200 Ma, with a reduction in bacterial sulfate reduction (BSR) and the emergence of active bioturbators being suggested as factors in this change. This study aims to assess the hypothesis that the change in color was primarily driven by changes in the rate of BSR, in which the loss of abundant gray carbonates was associated with a decline in pyrite deposition in marine sediments. Here, the bulk

geochemistry of marine carbonates was analyzed using a handheld XRF Tracer. These rock samples include ~ 679 Paleozoic and Mesozoic carbonates that had previously been characterized for their color, depositional environment, and bio-stratigraphic age. Exploratory statistical methods, including Random Forest, PCA, and RDA, were then used to identify correlations between carbonate chemistry, color, age, and depositional facies to identify whether pyrite was the dominant colorant in black and dark gray carbonates. Based on the resulting models, the most dominant directions of geochemical variation are between carbonate-pure limestone and terrigenous material-rich marls. Rock color is not strongly associated with sulfur content or other evidence of hypoxia. The statistical analysis does not support the hypothesis that pyrite abundance controls carbonate color, thereby implying that other processes outside of changes in BSR were the driving mechanisms behind the observed changes.

INTRODUCTION

One of the oldest observations in the field of geology and stratigraphy is that Paleozoic carbonates older than ~ 200 Ma are nearly universally black to dark gray in color while the majority of younger ones are tan to white, with dark colored carbonates largely disappearing from the record after ~ 100 Ma. This temporal trend in color is so widespread that it has been observed across multiple continents, including Europe and North America (Ager 1973). However, despite how significant this observation was in the early years of geology, there have been few studies that sought to quantify the change in color of marine carbonates across time or identify the driving forces behind this widespread transition.

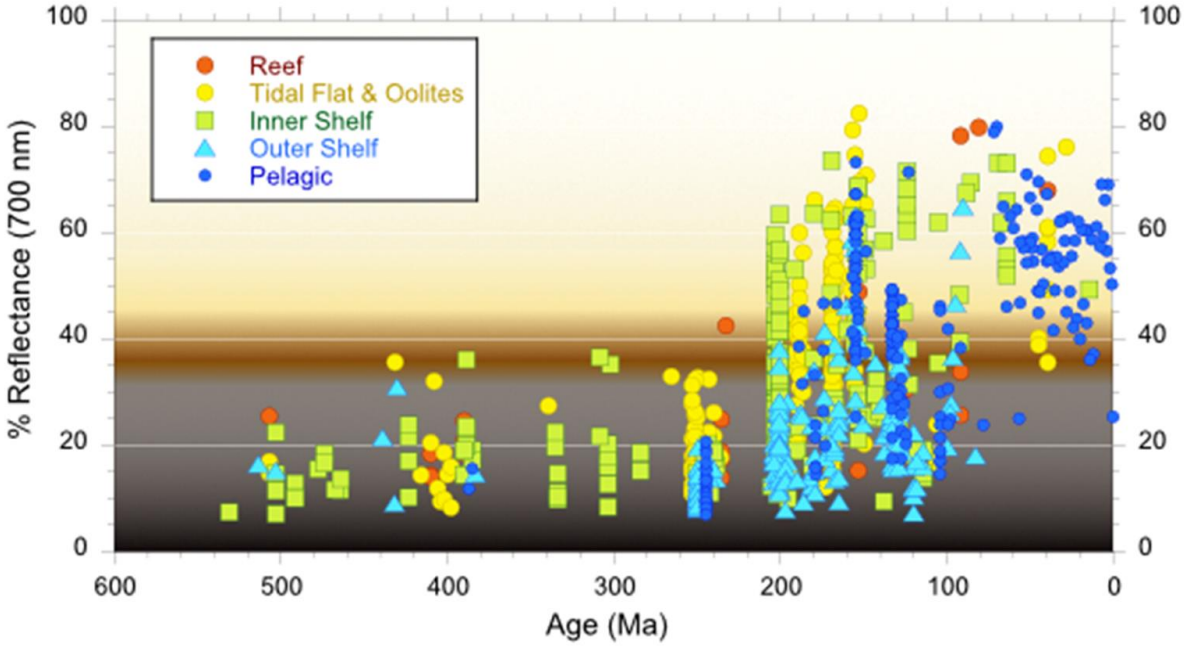

Figure 1: Sample age vs. reflectance at 700 nm from Rishi K Sugla and Richard Norris (Sugla 2021). Colors in the background approximate the sample color. Note the emergence of lighter-colored, high reflectance carbonates after ~200 Mya, and the disappearance of dark, low reflectance carbonates after ~ 100 Mya.

One study that addressed both topics comes from Rishi Sugla. In his unpublished thesis 2018 paper *Secular trends in Phanerozoic carbonate sediment color and ocean oxygenation*, Sugla hypothesizes that the changes observed in marine carbonate color over the past 500 million

years reflect the progressive oxygenation of the Earth's deeper oceans, from reducing conditions in the Paleozoic to oxidizing conditions in the Mesozoic and Cenozoic. He argues that as the Earth's oceans became increasingly well oxygenated, two major changes took place. First, the dominant metabolic pathway in marine sediments shifted from bacterial sulfate reduction (BSR) to O_2 reduction about 200 million years ago. This shift would have reduced the formation of framboidal pyrite (FeS_2), a biogenic form of pyrite that, when abundant, turns sediments black or gray (Berner 1984). Second, the increased availability of O_2 enabled the evolution of actively burrowing infauna. These burrowing animals directly consumed buried organic matter, which is typically dark brown in color, while simultaneously ventilating sediments via their burrows, further improving sediment oxygenation and iron oxidation (Thayer 1983). The combination of these two O_2-driven processes would be sufficient to explain why marine carbonates develop oxidized colors in the Mesozoic, thereby making color an indirect proxy for marine oxygenation through the Paleozoic and Mesozoic.

To test this hypothesis, Sugla quantitatively measured the color of marine carbonates spanning the last 500 Ma, using a spectrophotometer on polished thin section blanks of marine carbonate rocks. He used the percentage reflectance at 700 nm as a representative wavelength to describe sediment color. He then plotted their results against time in order to identify the major trends in carbonate color over the Phanerozoic. The resulting plot is shown in Figure 1. White and tan carbonates only appear in the sample record after ~ 200 Mya, and by ~100 Mya, black and dark gray carbonates nearly completely disappear from the record. If carbonate color is a valid proxy for marine O_2 content, then this suggests that the oceans experienced widespread oxygenation that started around 200 Mya and reached modern levels by 100 Mya.

This interpretation is supported by several other marine O_2 proxies. Studies of iodine-calcium ratios (I/Ca) and δ^{98}Mo indicate a potential increase in marine O_2 around 200 Mya, as shown in Figure 2a (Lu et al 2018; Dahl et al 2010). Furthermore, several studies investigating bioturbation rates in marine sediments and the mobility of marine animals suggest that more active marine animals only began to appear after 200 Mya (Thayer 1983; Figure 2b).

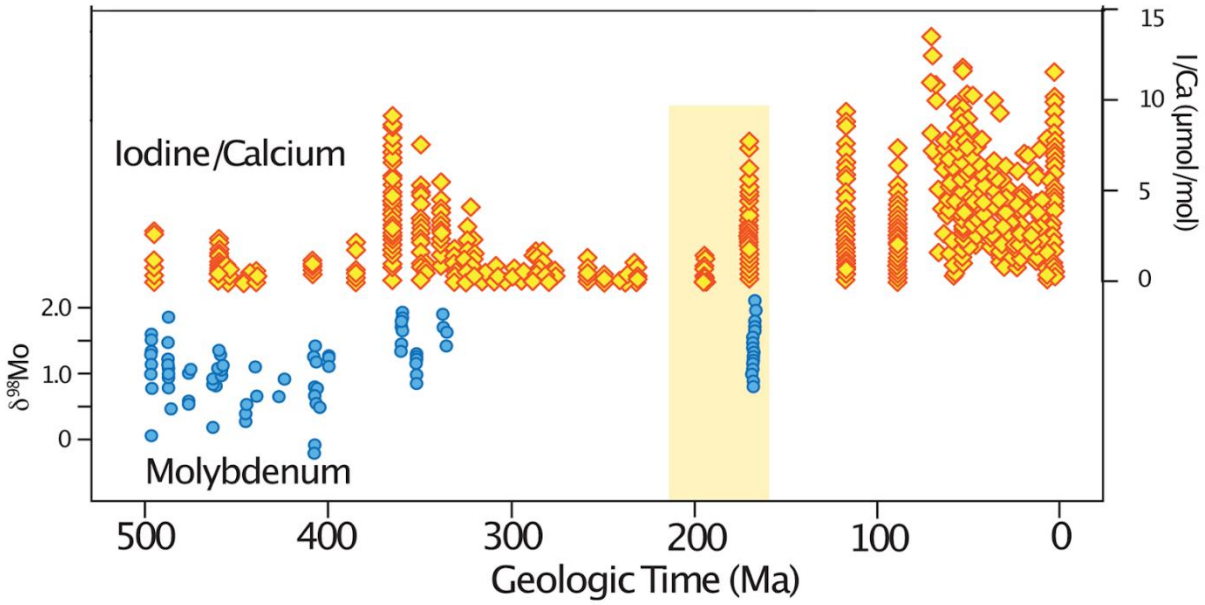

Figure 2a: Graph displaying the I/Ca ratios and δ^{98}Mo values of marine carbonates over the past 500 Mya. Higher I/Ca and δ^{98}Mo values are both linked to higher dissolved O_2 content in seawater. Note the highlighted section around 215-160 Mya, in which both I/Ca and δ^{98}Mo display elevated values, suggesting that the oceans underwent a period of oxygenation during the early to mid-Mesozoic. I/Ca data from Lu et al. 2018, δ^{98}Mo data from Dahl et al. 2010, graph produced by Dr. Richard Norris.

The emergence of active burrowers and larger, more mobile marine fauna around this time further supports the proposed oxygen hypothesis, as more active animals need more O_2 for respiration (Thayer 1983). This combined evidence implies that the oceans experienced a widespread oxygenation event around 200 Mya, which appears broadly consistent with Sugla's hypothesis. That said, these proxies don't provide insight into whether the change in carbonate color was mediated primarily through BSR or organic matter (OM) preservation.

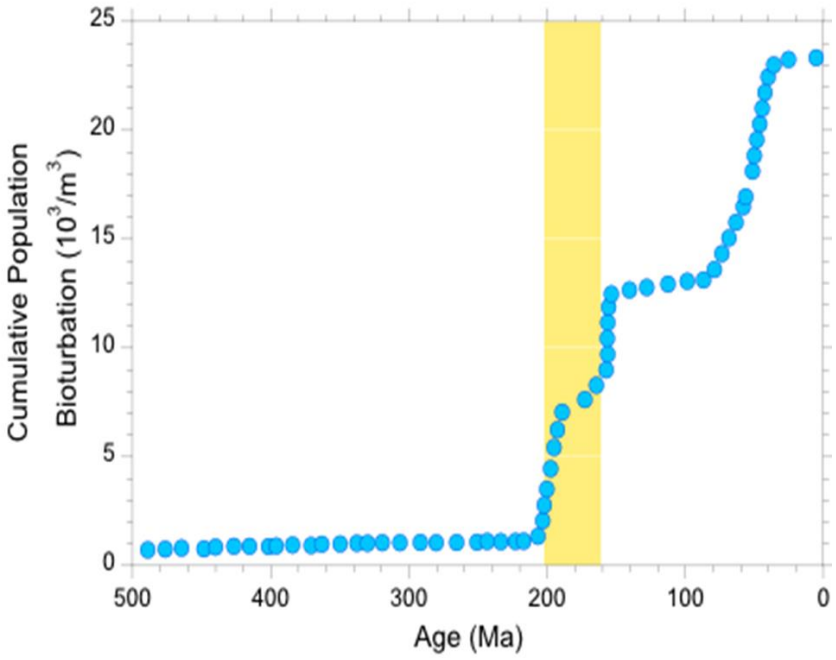

Figure 2b: Changes in Cumulative Population Bioturbation over the past 500 Mya. Note the highlights section, which indicates a period around 200 Mya when rates of bioturbation began to increase significantly from Paleozoic rates. Data from Thayer 1983, graph reproduced by Dr. Richard Norris.

This study aims to assess one of the underlying assumptions of Sugla's hypothesis, specifically that the change in carbonate color was primarily mediated through changes in rates of BSR over the past 500 Mya. If this is the case, then it would be expected that black and dark gray carbonates would contain greater concentrations of framboidal pyrite, which in turn should be reflected in the bulk geochemistry of the carbonate samples (i.e., darker samples having higher concentrations of Fe, S and other sulfide-forming elements) (Calvert and Pedersen, 1993). To address this question, the bulk geochemistry of the majority of carbonates from Sugla's sample set was semi-quantitatively characterized for their major element and limited trace element content. These data were used in combination with the reflectance and age data from their analysis to construct a series of statistical models designed to test for systematic variations in bulk geochemistry through time.

If the color in gray and black samples comes from framboidal pyrite produced via BSR, then the data should display the following: First, black and dark gray samples should display

higher concentrations of sulfur (S) and iron (Fe) than lighter samples due to the inclusion of framboidal pyrite. Second, older samples should contain more S and Fe than younger samples. This follows from the observation that older samples tend to be darker than lighter samples, as demonstrated by Figure 1. Finally, darker samples should contain higher concentrations of elements that form sulfide minerals in marine sediments, such as copper (Cu) and zinc (Zn) (Calvert and Pedersen, 1993). If none of these trends are observed within the data, then it is most likely that pyrite is not the primary colorant in darker carbonates, and another component, such as organic matter (OM), is more likely to be the primary driver behind color. This study tests for these trends using a series of statistical models, including Random Forest, Principal Components Analysis, and Redundancy Analysis.

METHODS

The samples selected for this analysis originated from the collection used by Rishi K. Sugla for his thesis project (Sugla, 2021). The samples reflect a variety of environments, from shallow reefs to the deep ocean, and range in age from ~ 40 Mya to ~ 513 Mya. Geologic sample environment was determined by Sugla based upon microfacies analysis of each specimen together with literature review. Color reflectance was measured using a desktop spectrophotometer in Dr Kathy Barbeau's laboratory at Scripps Institution of Oceanography. The percentage of reflectance at 700 nm was chosen as a proxy for color based on the maximum divergence of samples at this wavelength. Most samples were previously cut and polished as thin

Figure 3: Photograph of three carbonate samples, prepared as 1-inch polished rock chips. Samples pictured display the range of colors present within the sample set. The oldest samples, i.e. Paleozoic, tend to be dark black to gray in color, similar to the leftmost sample below. Samples showing intermediate (brown, medium gray) and light (tan to white) colors only begin to appear in the Mesozoic.

section blanks by Rishi Sugla for spectrographic color analysis and did not need to be re-prepared for XRF analysis. Samples were sliced into ~3 x 5 cm chips about 1 cm thick with a tile saw and subsequently hand polished with 500 grit (~15-20 μm) sandpaper to remove saw marks

and create a uniform, smooth surface on one side (Figure 3). All samples that required re-polishing were allowed to dry for at least 2 hours before being scanned using a handheld XRF.

Estimates of the geochemical composition of each sample were collected using a handheld Bruker Tracer 5i XRF. Weight percent element (%Wt) values were collected using the Earth Cal program (50kV, 10µA), using an exposure time of 30 seconds, a beam diameter of 8mm, and an air-filled chamber. The Earth Cal program is a custom calibration program initially designed for analyzing the geochemistry of mudstones and was selected due to the limited availability of other calibration programs at the time of data collection. The resulting geochemical data were matched with previously collected data for 700 nm reflectance, sample age (based largely on biostratigraphy), location of collection, and depositional environment data, leading to a total number of 679 matched samples. In cases where the concentration of an element in the sample was below the detection limit (<LOD), a value of 0 was substituted in order to allow for compatibility with the random forest, PCA and RDA algorithm, which require numerical values in order to properly run.

The accuracy and reproducibility of the Bruker XRF was assessed using two tests. The first test involved assessing the accuracy of the handheld Tracer by comparing the data it collected to a series of pressed pellets (suitable for XRF) of geological reference materials produced by the MyStandards company. The product information sheets containing the assigned element values for each sample are provided in the supplemental files for this text. The following standards were chosen for this test: GH-NP (Granite), ECRM-752-1-HF, (Limestone), SdAR-L2-P (river sediment, low heavy metal pollution), and SdAR-H1-P (river sediment, high heavy metal pollution). The accepted values for major and trace elements for these standards are given in

Tables 6-9 in the Appendix, alongside digital links to the product information sheets for each standard.

The second test was designed to assess whether the handheld Tracer returns variable counts depending on how long the X-ray tube has been active, i.e. whether it displays a warm-up curve. Five samples were selected for this test. The samples selected included a light-colored sample, a dark-colored sample, a high-Ca sample, a high-Si sample, and a high-Fe sample. These samples were not reference standards but rather representative samples that serve only as a means to evaluate the reproducibility of the XRF data. Each sample was scanned a total of 19 times in a rotating sequence to produce a time series. The scanning started within the first minute of turning on the Tracer XRF and continued every 5 minutes for 2 hours. The results of these scans were also used to identify which elements had sufficient resolution and reproducibility to be used in exploratory statistical analyses. Several element %WT values were excluded as they were poorly measured by the Tracer; excluded elements include sodium, magnesium, phosphorus, copper, cobalt, vanadium, niobium, molybdenum, lead, thorium, and uranium.

The elemental data were first analyzed via Random Forest analysis using the randomForest R package. Random Forest is a machine learning method that partitions data into several smaller bags and tests a predictive model against each bag, producing a collection of decision trees. The results of these trees are then averaged together in a group-voting process, which is done to reduce the impact of overfitting on the data (i.e. the tendency of the algorithm to identify nonexistent patterns when it runs for too long) (Brieman 2001). For the Random Forest analysis, elements displaying percentage increases in mean standard error (%IncMSE) greater than 10% after a max tree number (mtry) optimization were used to construct a second, limited model. The results of the Random Forest analysis were assessed based on two metrics:

percentage increase in mean standard error (%IncMSE) and increase in node purity (IncNodePurity). %IncMSE is the increase in the mean standard error of the model when a variable–such as an element, geologic age or sediment color– is removed from the set of explanatory variables. IncNodePurity represents the change in the simplicity of each decision tree when variables are removed as measured by the number of branches at each decision step, or "node", with fewer branches equating to greater purity.

Next, the data were analyzed using two additional methods, PCA (Principal Component Analysis) and RDA (Redundancy Analysis), using the vegan R package for both. PCA is an ordination method that resolves data into the major axes of variation. This grants PCA an advantage over other similar methods, as it can identify multiple directions of variation rather than just the dominant direction within a data set. For the PCA analyses, the first model incorporated the entire elemental data set. Elements displaying strong positive or negative species scores (> +1.0 or < -1.0) in principal components 1 through 6 of this whole-element model were selected for further review and use in two subsequent models: an element-only model (EO) and an element-color-time model (ECT). The element-only model contains the Wt% data for elements that showed consistency and reproducibility in the time tests. The element-color-time model contains all the data from the element-only model, with the addition of the age (time) and reflectance (color) data from the color spectrophotometer analysis. The resulting principal components (PC) of the EO and ECT models were then evaluated for importance using the Keiser-Guttman criterion, which states that components with an Eigenfunction Score equal to or greater than 1 should be considered significant (Gortezko and Bühner, 2022). Principal components (PC) that were deemed significant were then used to construct a series of site-score scatterplots and eigenvalue biplots that were then used to interpret the results of each PCA.

For RDA analyses, a forward selection method was used to identify which elements were statistically significant, both when modeling carbonate color as a function of elemental composition alone and as a function of both elemental composition plus each sample's geologic age. The resulting optimized models were then built and their adjusted R^2 values derived. Significance tests for both the timeless and time-included RDA model were performed, the results of which are reported below. Due to the structure of the data, no biplots could be constructed using the RDA results.

RESULTS

Comparison to Geologic Standards: For the initial comparison test, the Granite standard, GH-NP, was selected as its chemistry is the most similar to terrigenous sediments produced by continental weathering, which is an expected component in marls along with the terrestrial-sourced components of relatively pure calcium carbonate. Major elements for the standards were initially reported as oxide weight percents and were therefore recalculated as elemental percentages so that major and trace element data were internally consistent (as elemental percentages). The adjusted values were then plotted alongside the XRF results on a logarithmic scale as a series of scatter plots, shown in Figures 4a - 4d and the Appendix Tables 6-9.

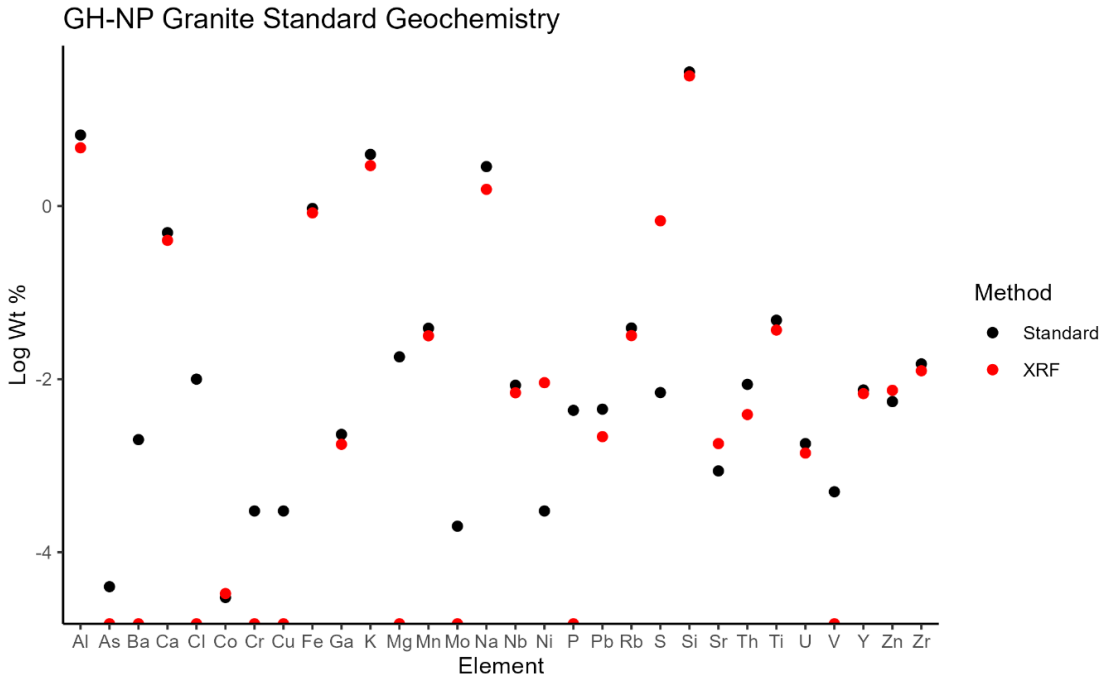

Figure 4a: Comparison of known and estimated element concentrations for GH-NP, a powdered granite standard. Known values are shown in black, average of three XRF scans shown in red.

For most major elements, the Bruker Tracer XRF appears to be relatively accurate with the exceptions of Na and Mg, where the XRF results are several orders of magnitude different

from the expected standard values. This is likely because these elements were too light to be reliably detected in an air-filled chamber of the Bruker Tracer XRF. The XRF results for the trace elements are also less accurate, especially for the transition metals and S. For the transition metals, this may be due to the low detection limit of the Bruker Tracer XRF, which appears to be between 0.003 and 0.001 Wt%.

For the second round of comparison tests, which was conducted after purchasing a new set of standard samples from Mystandards, three standards were used, ECRM, SdAR-L2, and SdAR-H1. ECRM is a limestone sample, while SdAR-L2 and SdAR-H1 are both riverine sediment samples with differing levels of heavy metal and pollutant contamination (low contamination and high contamination respectively). These standards were selected for being sedimentary rocks, and therefore closer in composition to the samples used in this project than the initial GH-NP granite standard. The same procedure used in the initial comparison test was repeated for each of these three samples, and the results are given in Figures 4b – 4d.

The results of these additional tests appear to show that the Tracer is relatively accurate when it comes to assessing the concentrations of the major elements, particularly Ca, Si, Fe, Al, and Mn, as well as a select number of trace elements, including Mn, Sr, and Zr. As for the discrepancy in S seen in Figure 4a, further investigation will be required to determine whether this is due to matrix interference or if it is the result of a miscalibration in the EarthCal program used by the Bruker Tracer. However, the results of the warm-up tests, discussed later in the text, seem to imply that the Tracer is relatively consistent at detecting S in marine carbonates (Figure 5f)

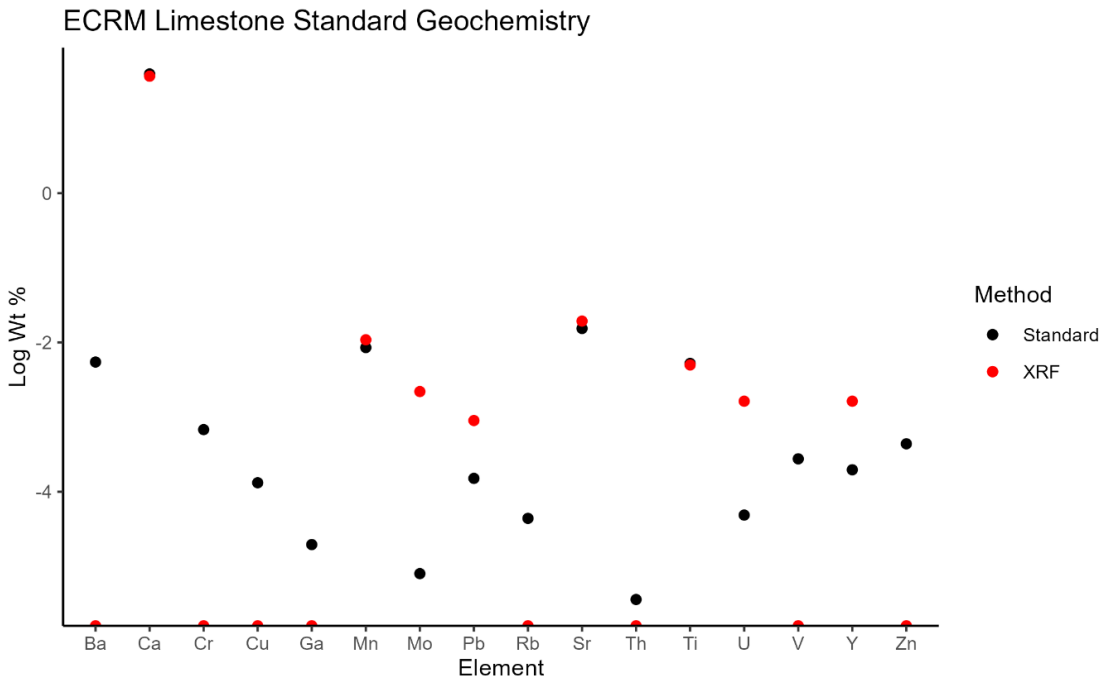

Figure 4b: Comparison of known and estimated element concentrations for ECRM, a powdered limestone standard. Known values are shown in black average of three XRF scans shown in red.

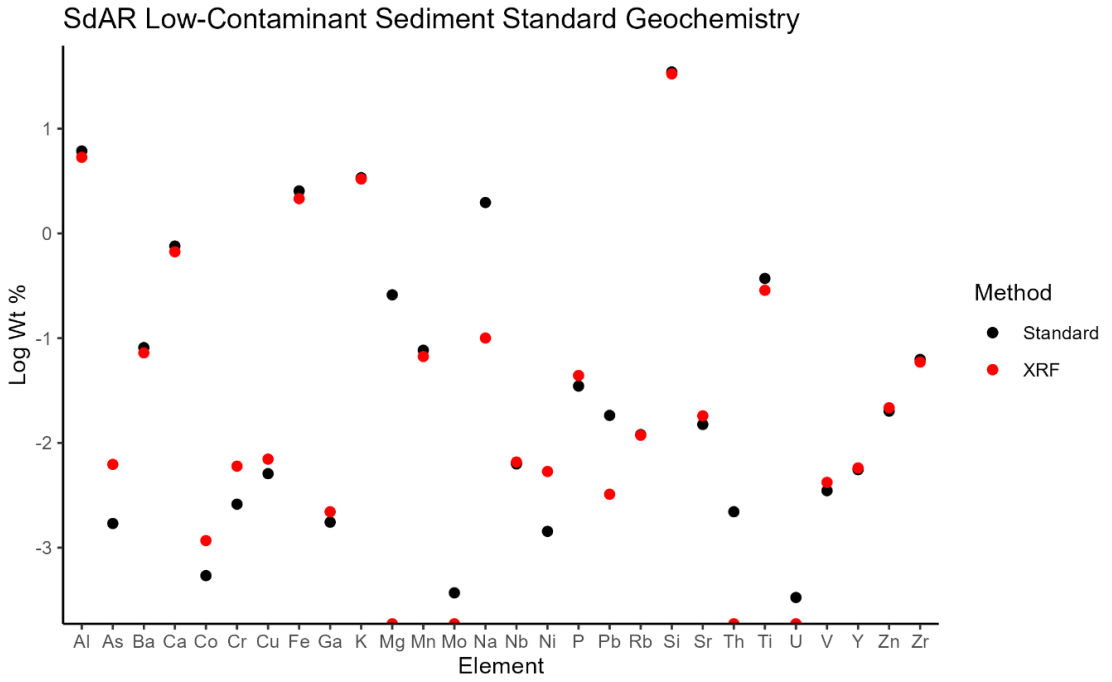

Figure 4c: Comparison of known and estimated element concentrations for SdAR-L2, a powdered riverine standard with low pollutant contamination. Known values are shown in black, average of three XRF scans shown in red.

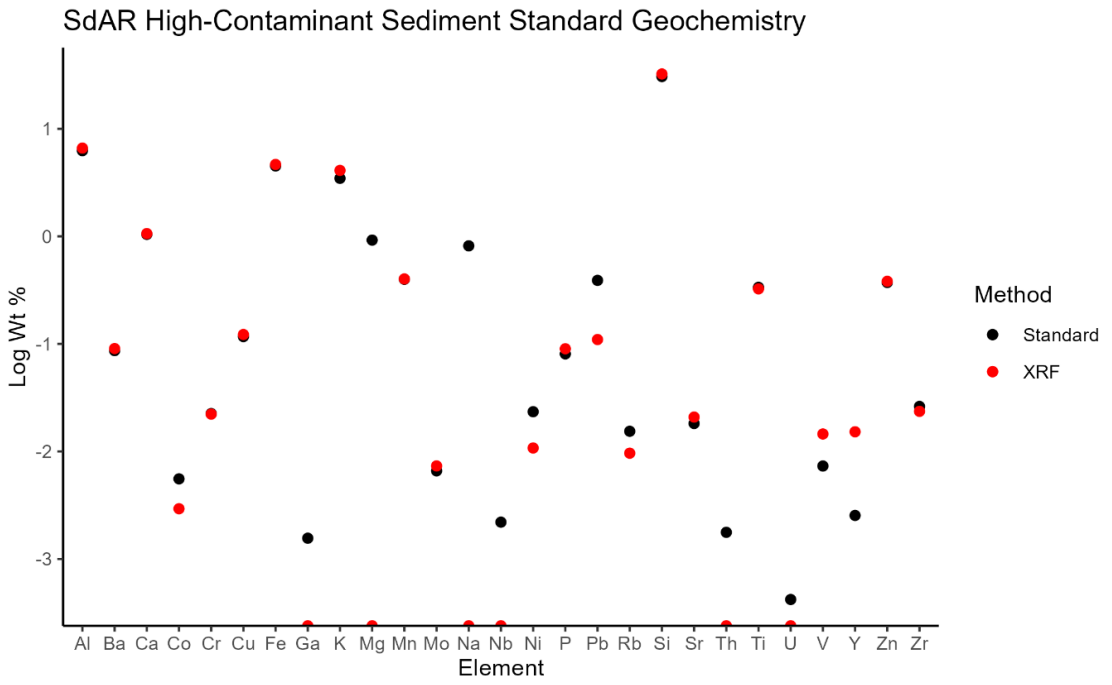

Figure 4d: Comparison of known and estimated element concentrations for SdAR-H1, a powdered riverine standard with high pollutant contamination. Known values are shown in black, average of three XRF scans shown in red.

Warm-up Test: The results of the time tests were plotted against time for several major elements, as well as some trace elements of inquiry, to assess whether the quality of the data was sufficient for later analyses. Elements displaying relatively consistent measurements and detection at each time step were deemed high-quality for the purposes of this analysis. Elements that displayed inconsistent detection were deemed unusable.

The analysis did not reveal a clear signal of lower counts during the initial 15-20 minutes after turning on the XRF tube. Certain samples, namely VB-26 (Figure 5b) and RS-0026 (Figure 5a, 5c), showed some variation in detection for certain elements, though this is most likely due to the Bruker handheld Tracer capturing small heterogeneities in the material, such as individual grains, during replacement of the samples on the detection window. However, there is poor reproducibility of counts for elements with low abundance. Several element %WT values were therefore excluded from the later analysis due to poor resolution and reproducibility. Excluded

elements include sodium, magnesium, phosphorus, copper, cobalt, vanadium, niobium, molybdenum, lead, thorium, and uranium. The results for a selection of these element tests are shown below in Figures 5a – 5f.

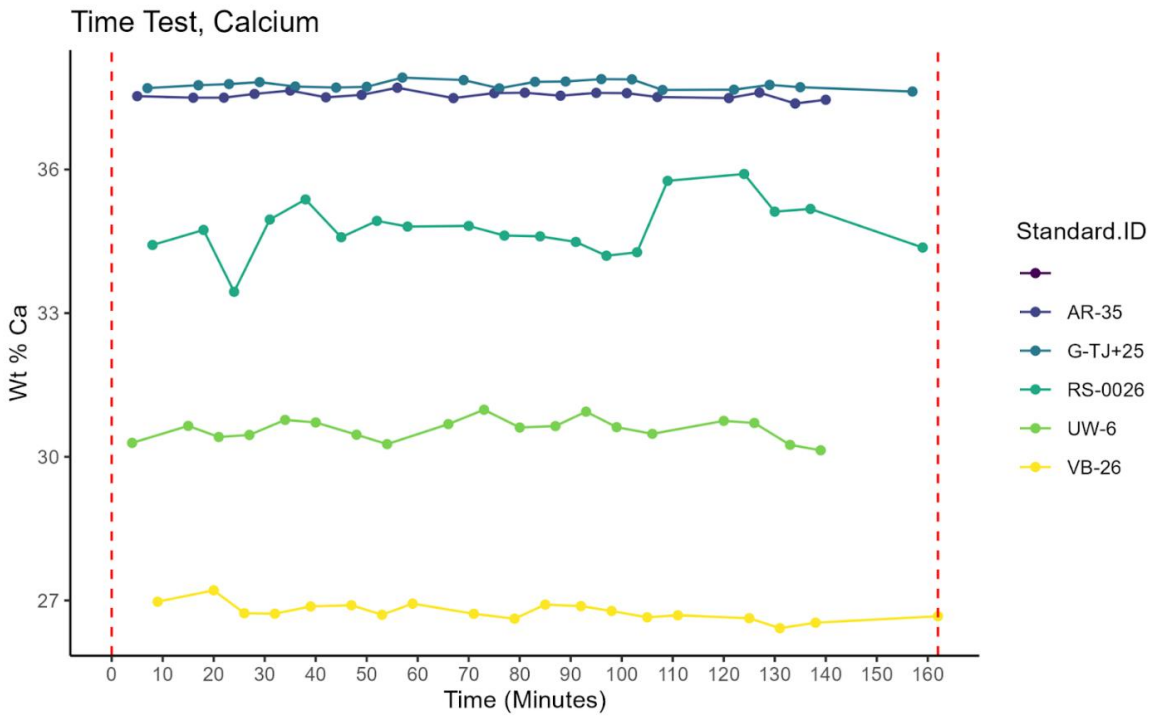

Figure 5a: Time test results for calcium. Reported WT% on the y axis, time series steps on y-axis. Time series steps were recorded in minutes. Red lines mark the activation and deactivation of the tracer. Note that the detection is relatively consistent across time, especially in comparison to other elements such as U (Figure 5d).

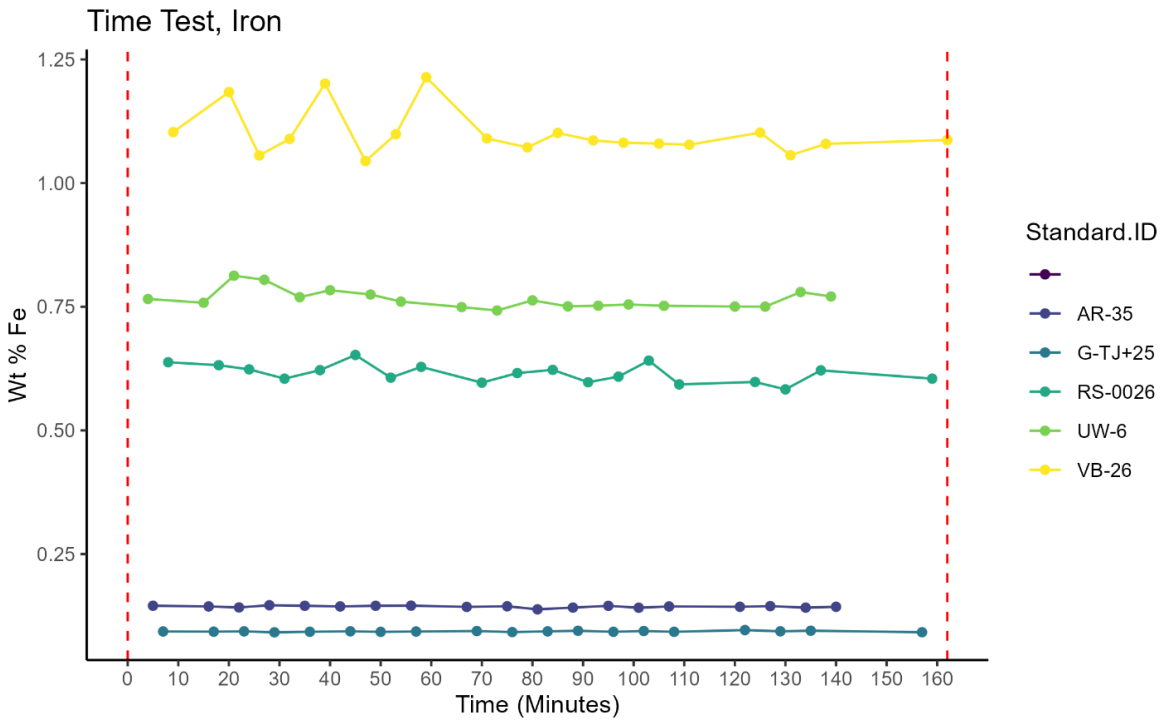

Figure 5b: Time test results for iron. Reported WT% on the y axis, time series steps on y axis.

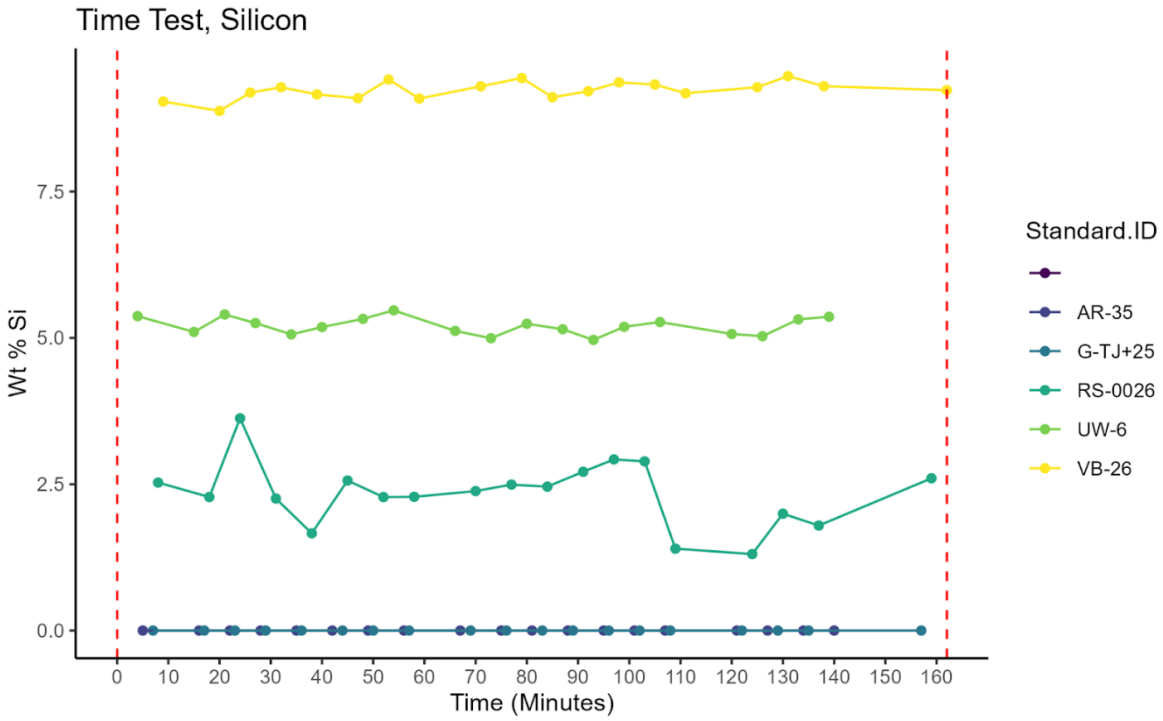

Figure 5c: Time test results for silicon. Reported WT% on the y axis, time series steps on y-axis.

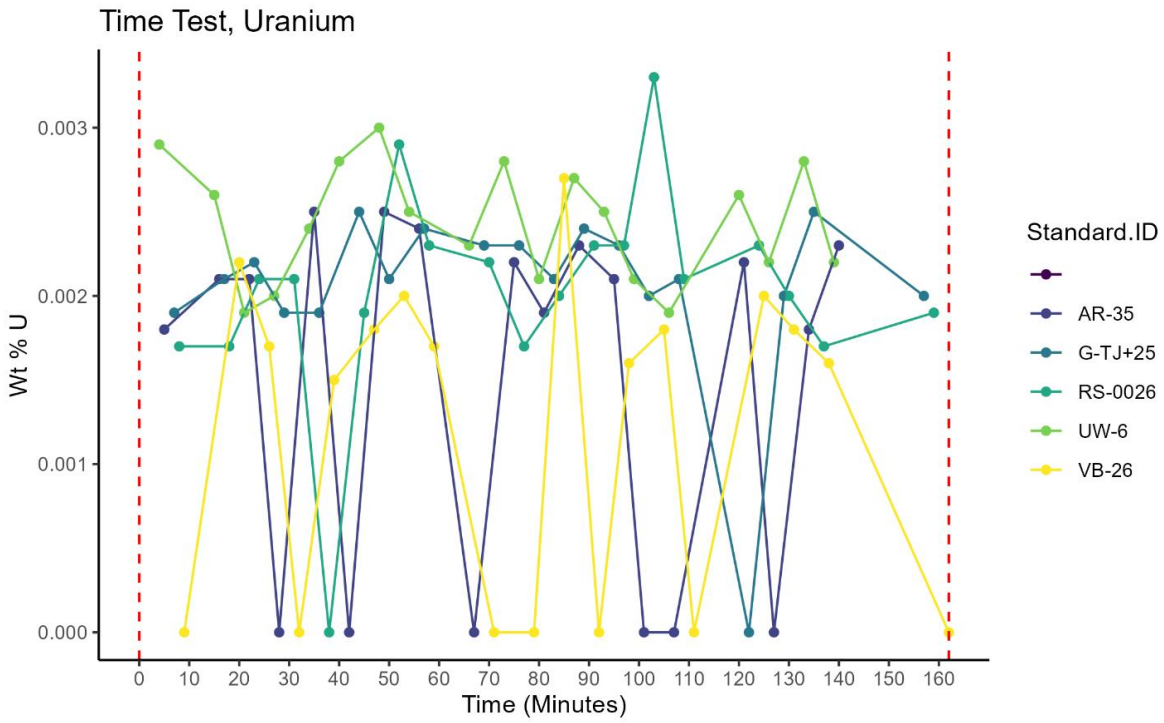

Figure 5d: Time test results for uranium. Reported WT% on the y axis, time series steps on y-axis.

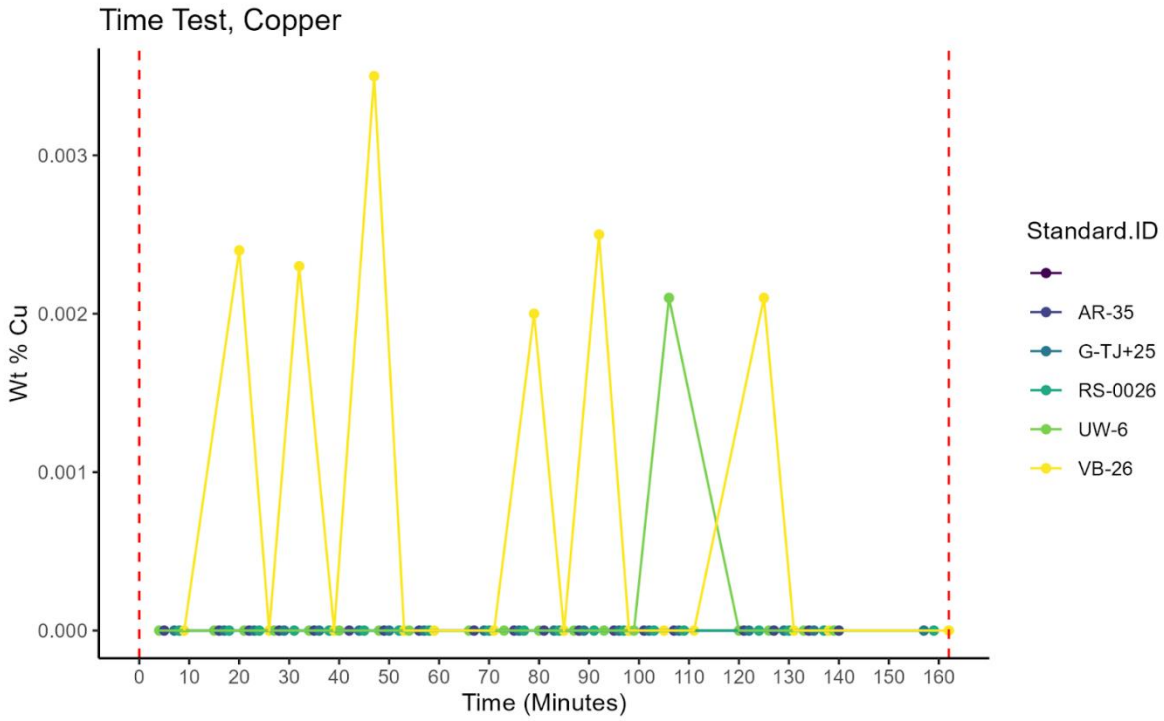

Figure 5e: Time test results for copper. Reported WT% on the y axis, time series steps on y-axis. Similar to uranium, the handheld tracer was often unable to detect the abundance of copper in the samples.

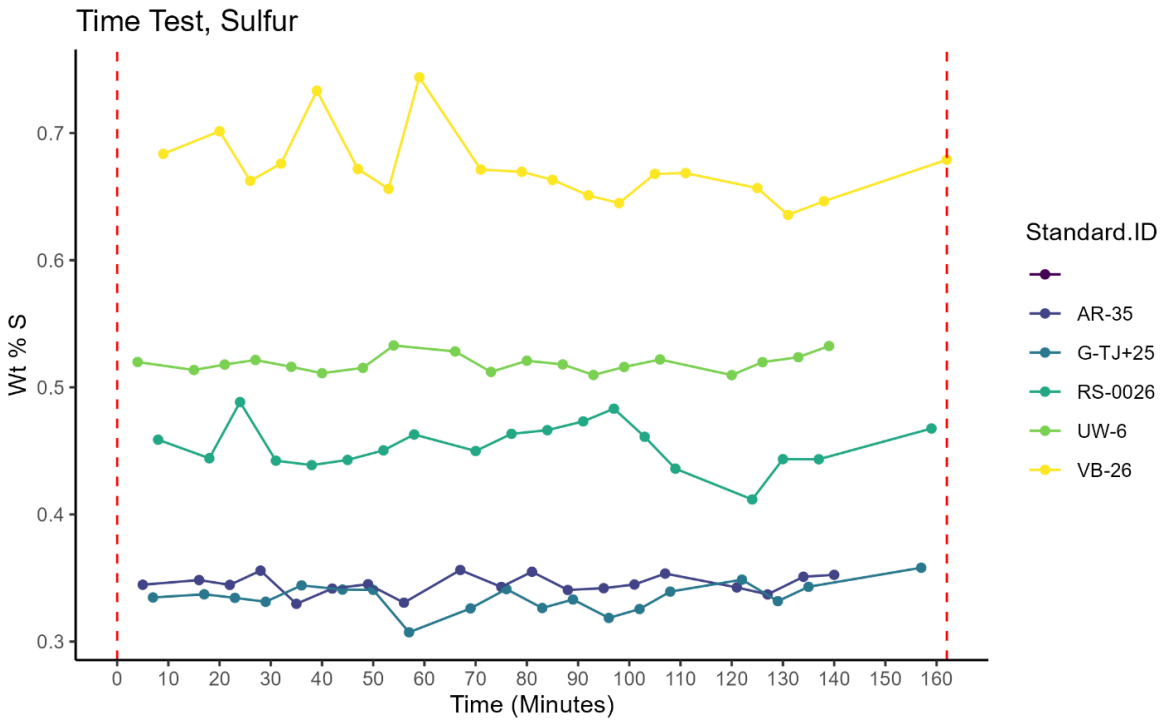

Figure 5f: Time test results for sulfur. Reported WT% on the y axis, time series steps on y-axis.

Random Forest: For the Random Forest analysis, the model was designed using a series of selected elements as well as sample age (Time) as predictors for sample color, as represented by reflectance at 700nm. Based on the results of this model, which are shown in Figure 6a, the age of the samples ends up being the strongest predictor of color, with all elements placing significantly lower in terms of their respective importance. For elemental species as explanatory variables only, the most significant elements in terms of percent variance explained are Sr, K, Ca, Ti, Sr, Y, Fe, Mn, and Si. These elements have been isolated from the other data and plotted in Figure 6b for clarity.

Overall, Sr, Mn, and Fe are the most significant values for the percentage of variance explained, as demonstrated by their percentage increase in mean standard error (%IncMSE) values of 45.97, 43.18, and 32.91 respectively. While Fe and Mn were significant in terms of their respective %IncMSE and change in IncNodePurity, Strontium (Sr) is the most significant predictor of all

elements across both metrics. Sulfur (S), meanwhile, is less significant across both metrics. The five most significant elements in terms of both %IncMSE and IncNodePurity are Sr, Mn, Fe, Si, and Ti. This suggests that these five elements are more closely correlated with each other in terms of their relationship to carbonate color, which is supported by the trends observed in the PCA analyses.

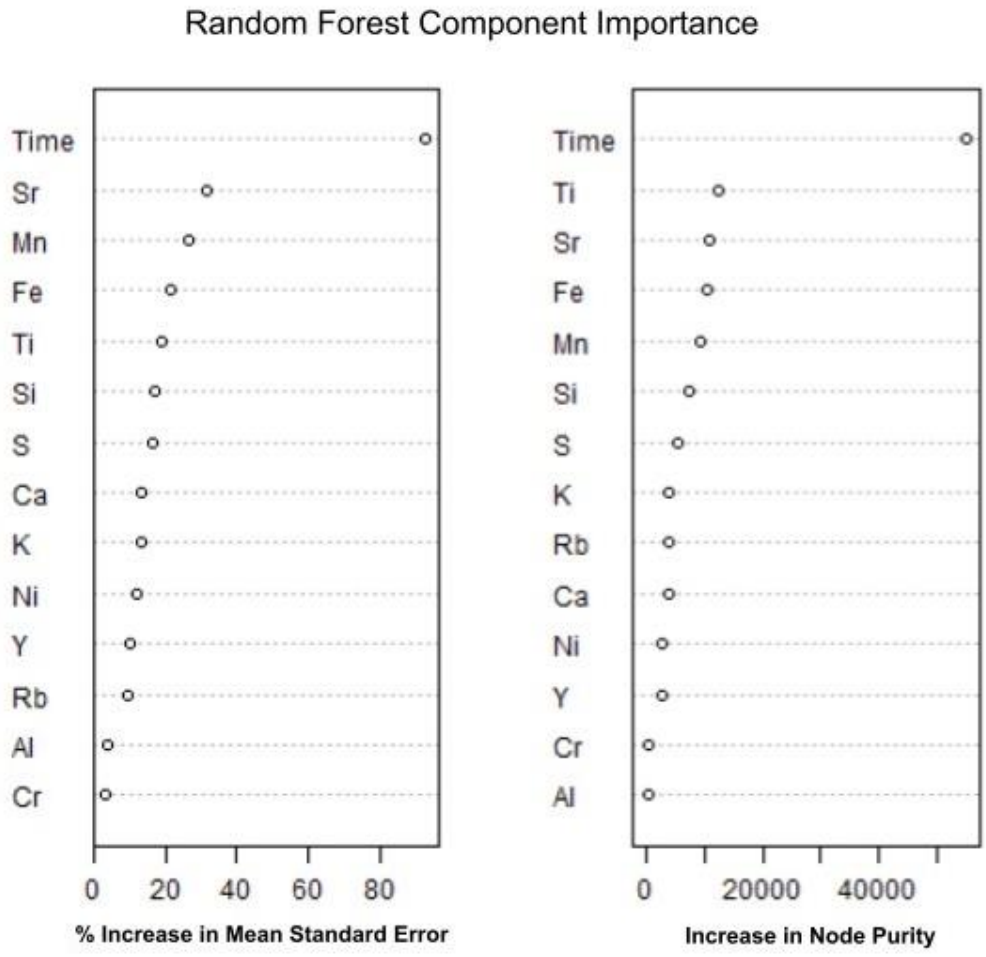

Figure 6a: Plots of the %IncMSE and IncNodePurity values for time and selected elements and sample age, from the initial Random Forest model. Note that time is the most significant variable across both metrics used.

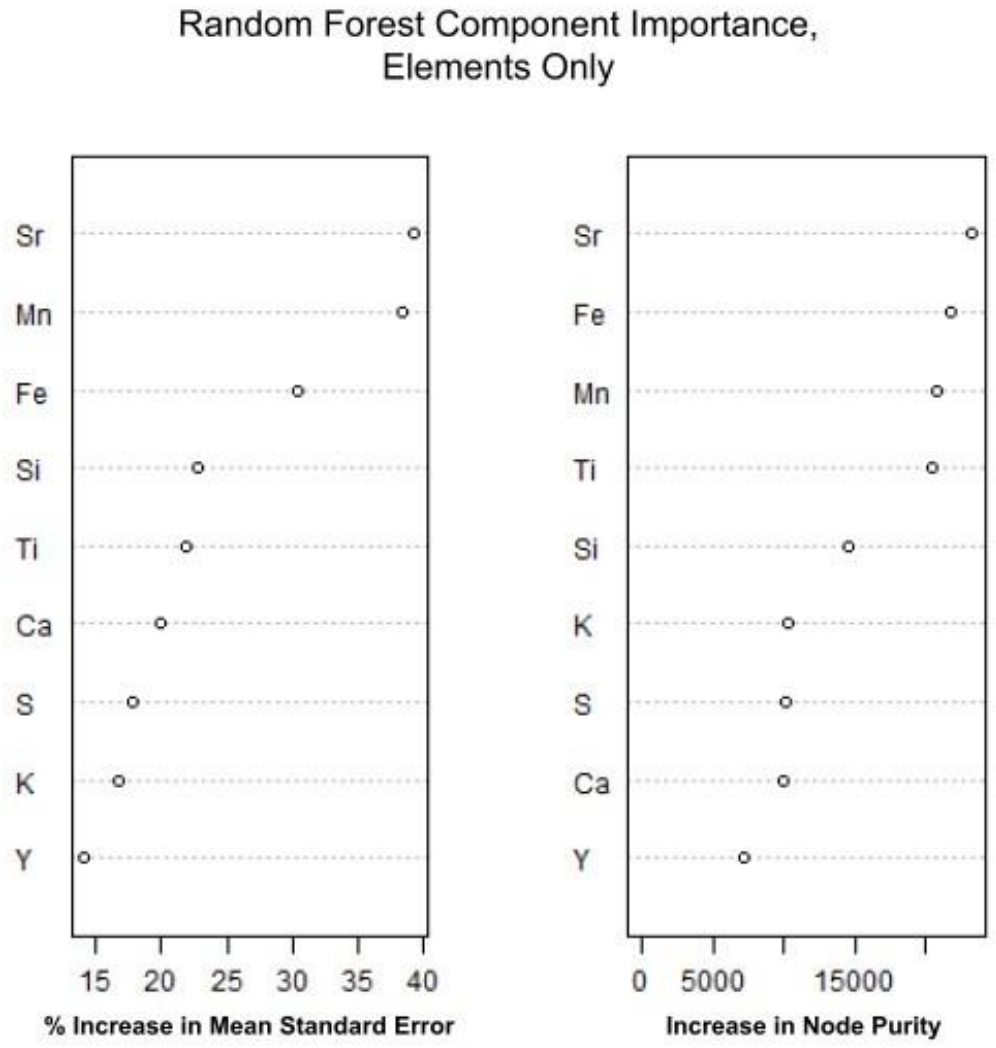

Figure 6b: Plot of the 10 most significant element species extracted from the initial Random Forest model. Sr, Mn, Fe, Ti, and Ca are the five strongest predictors when time is removed.

Element-only PCA: For the element-only (EO) PCA, the Kaiser rule analysis (Gortezko and Bühner, 2022) suggests that the first three PCs are significant (Eigenvalue > average PC value), with the fourth PC being slightly less than significant (Eigenvalue < average PC value). The results of these tests are given in Figure 7. After the EO PCA was constructed, the site and species scores and first four PCs, PC1, PC2, PC3, and PC4 were extracted. Site scores refer to the placement of individual rock samples along the PC axis. Species scores refer to the assigned

weight of each of the elements on each PCA axis. PCA site scatterplots and corresponding biplots were constructed using the extracted values. The resulting biplots (Figures 8 – 10) and a table of extracted species scores (Table 1) are given below. The circle of equilibrium contribution is also plotted on each biplot; eigenvectors that terminate outside of this circle are considered significant according to the PCA analysis.

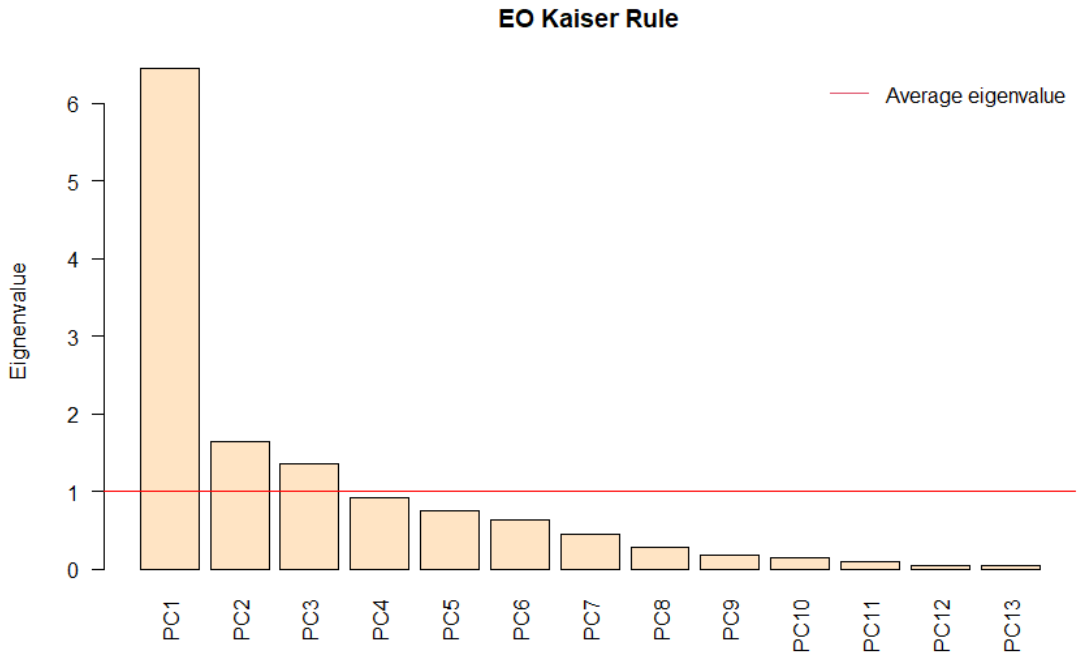

Figure 7: Barplot of results from the Kaiser-rule analysis performed on the EO PCA. Eigenvalues greater than the average eigenvalue are considered significant, in this case PCs 1-3.

According to the results of the EO analysis, the primary signal along the most significant axis, PC1, displays a strong anticorrelation between Ca (Eigenfunction Score > 2) and a suite of lithogenic-associated elements, namely Al, Si, K, Rb, and Ti (Eigenfunction Score < -2) (Table 1). These elements display strong anticorrelation on PC1 and moderate anticorrelation on PC2, with the strongest clustering of site scores being the clustering of Shallow marine/Oolite Shoal

rock samples towards the direction of the Ca eigenvector (Figure 8). The next largest signal is a strong Sr eigenvalue (Eigenfunction Score > 2) on PC3. When PC3 is plotted against PC2 and PC4, we can see that the Sr signal is associated of cluster of Outer Shelf specimens and shows covariance with Rb (Figures 9 and 10). Other notable features of the model include a strong Y signal on PC4 (Eigenfunction Score ~ -1.6), though this is likely due to a handful of outliers within the dataset that have otherwise been excluded from the plot, given the lack of any clustering in site scores along the direction of the eigenvector for Y in Figure 10b.

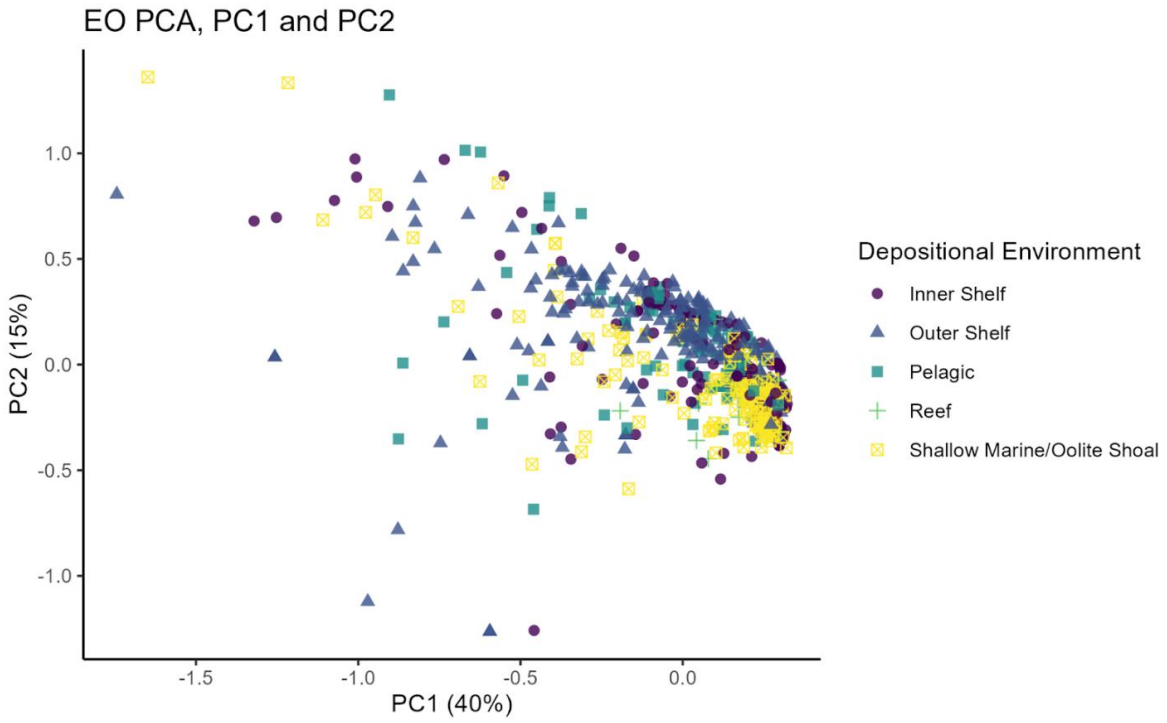

Figure 8a: Biplot of element-only PCA site scores for PC1 and PC2. The percentage of total variation explained by each PC is shown in the axis labels. The depositional environment of each sample is shown in the key on the right side of the graph. Site scores are plotted against PC1 and PC2 to identify clustering in the samples, though this biplot shows no significant clustering.

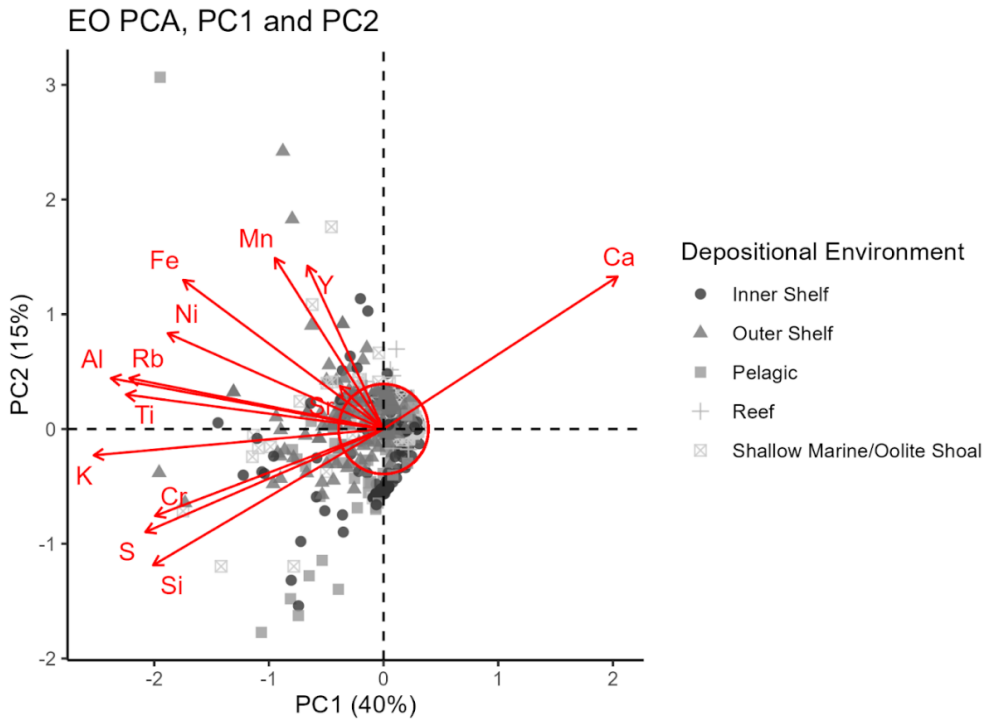

Figure 8b: Biplot of EO PCA for PC1 and PC2 with eigenvectors plotted in red. Circle of equilibrium is also displayed in red. Note the eigenvectors of Ca and Si; the opposing directions of these vectors indicates a strong anticorrelation between Ca content and Si content, likely reflecting a measure of carbonate purity.

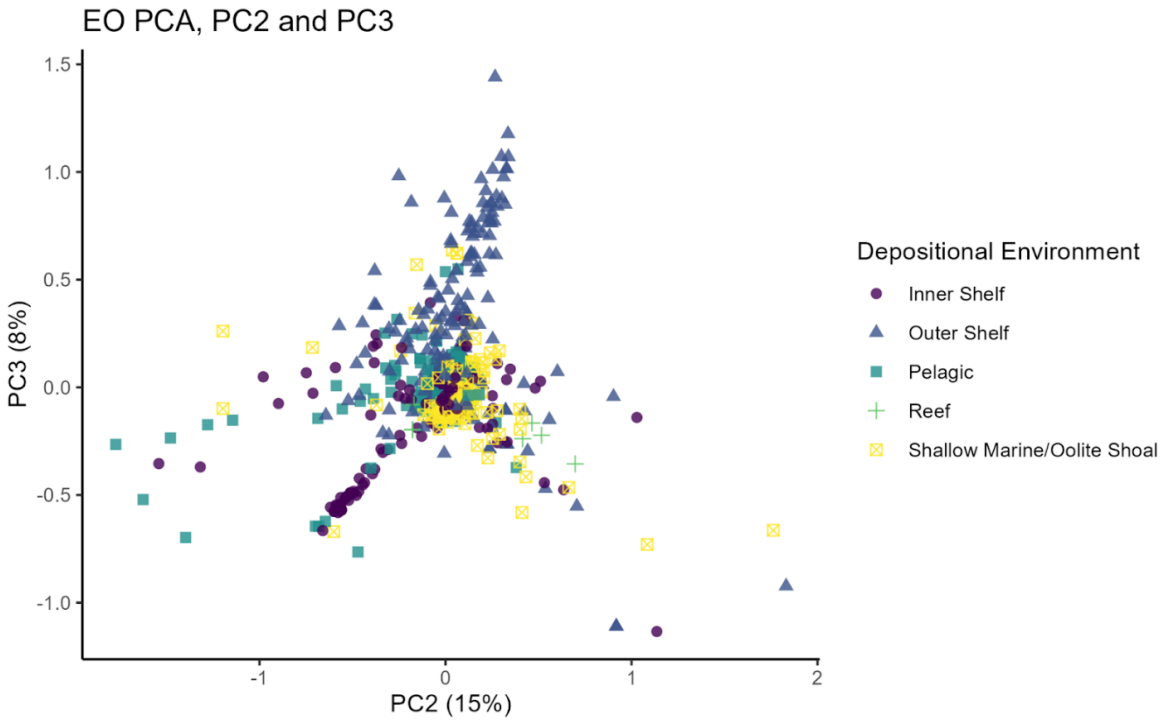

Figure 9a: Biplot of EO PCA site scores for PC2 and PC3. The percentage of total variation explained by each PC is shown in the axis labels. Note the elongated cluster of outer shelf samples in the upper right portion of the graph.

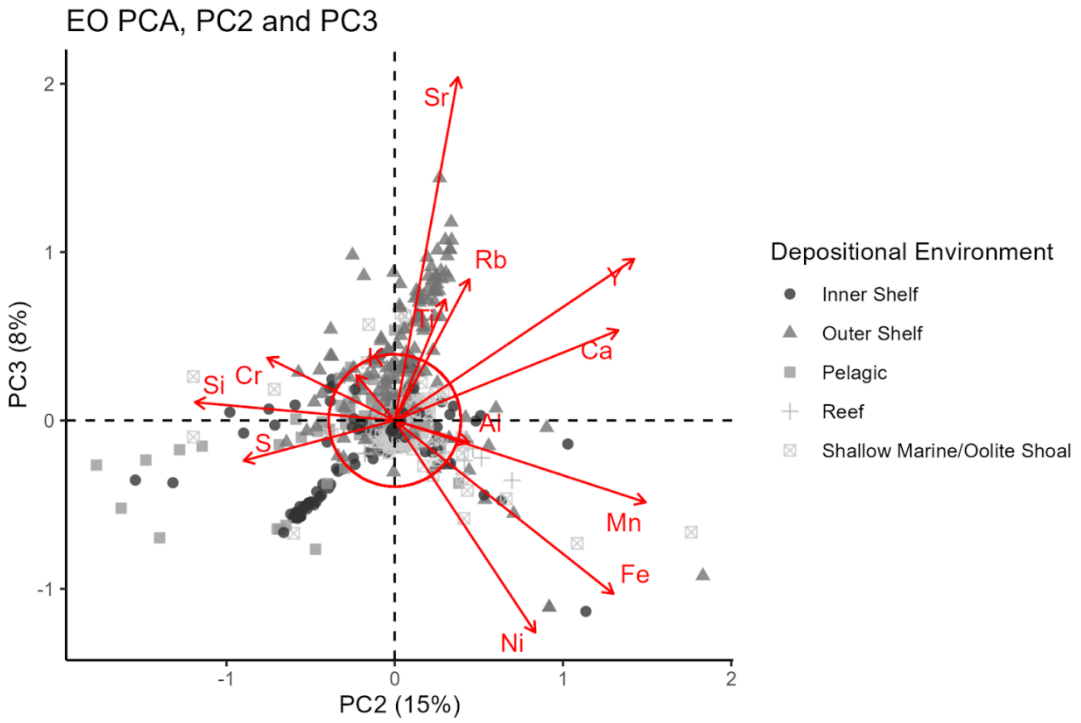

Figure 9b: Biplot of EO PCA for PC2 and PC3 with eigenvectors plotted in red. Circle of equilibrium is also displayed in red. The cluster of outer shelf samples noted in Figure 9a roughly aligns with the eigenvector for Sr.

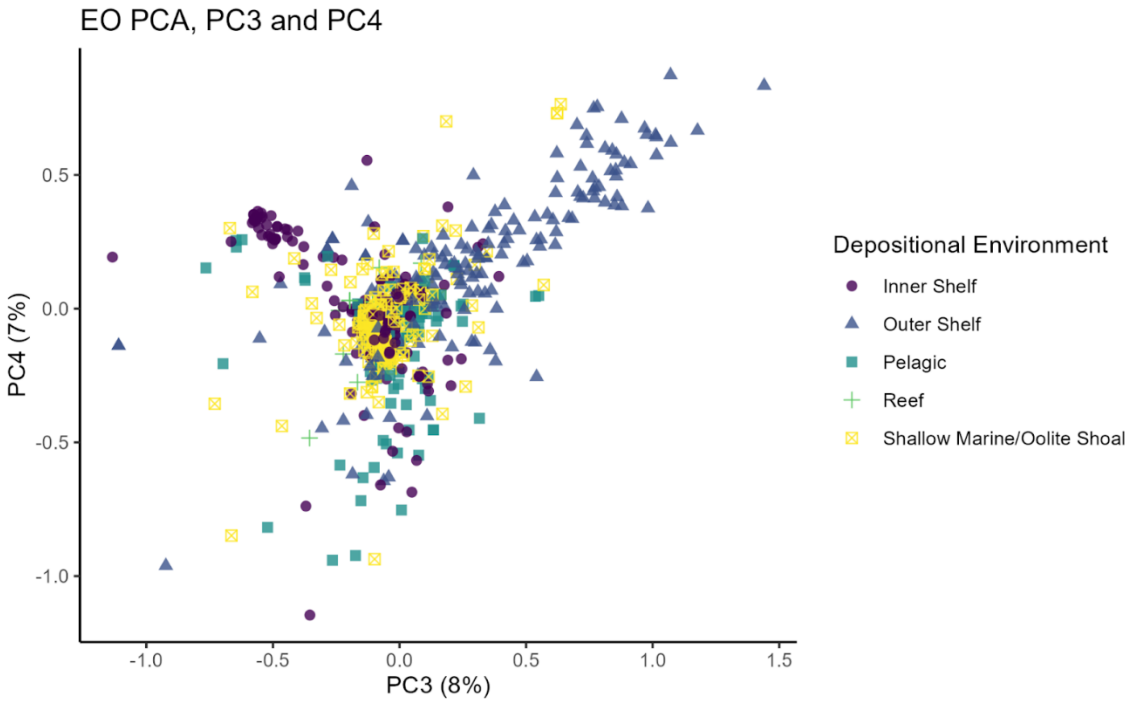

10a: Biplot of EO PCA site scores for PC3 and PC4. The percentage of total variation explained by each PC is shown in the axis labels, with these two PCs being relatively minor in terms of their significance. Like Figure 9a, there is loose clustering of outer shelf sediments, as well as tighter cluster of inner shelf sediments to the upper left.

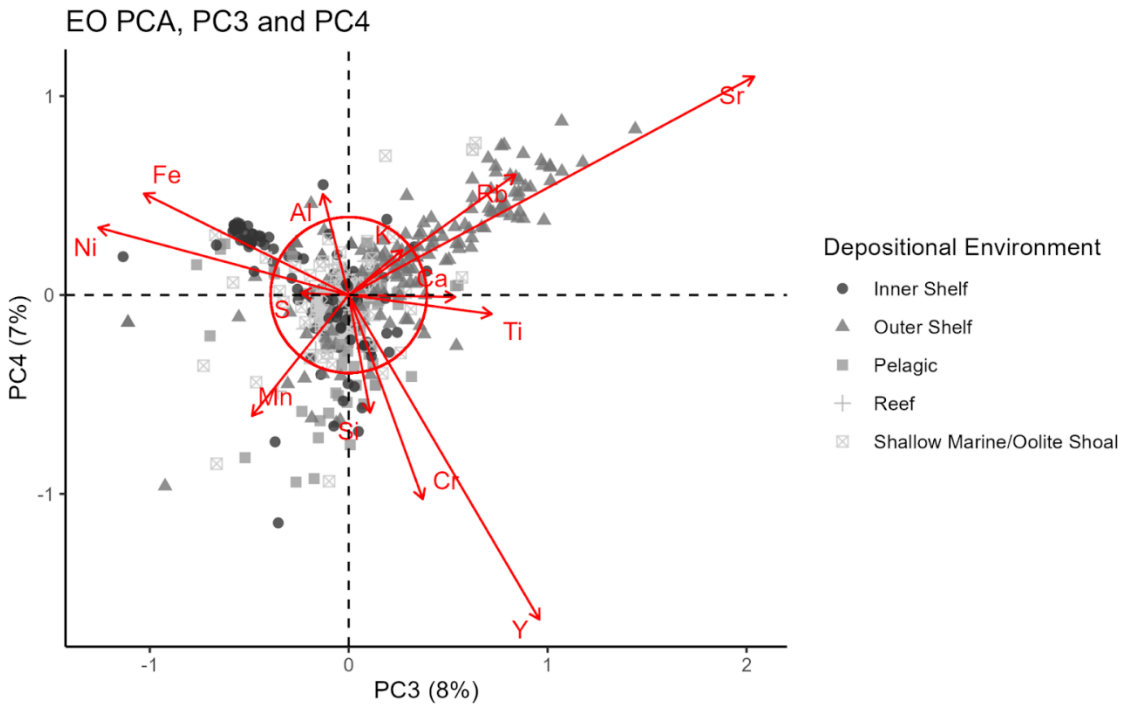

Figure 10b: Biplot of EO PCA for PC3 and PC4 with eigenvectors plotted in red. Circle of equilibrium is also displayed in red. The outer shelf cluster again aligns with Sr, while the inner shelf cluster lines up with the eigenvector for Fe.

Table 1: EO PCA eigenfunction scores for each element species, PCs 1 through 4. Values indicate the importance and relative orientation of each element along the axis, with higher magnitude scores indicating that the element is significant to the dimension described by the axis.

Element	PC1	PC2	PC3	PC4
Al	-2.3771373	0.4425441	-0.1299923	0.507049575
Si	-2.0094230	-1.1872165	0.1079255	-0.591528594
S	-2.0765798	-0.8979353	-0.2390273	0.008828692
K	-2.5273197	-0.2291665	0.2695565	0.225897745
Ca	2.0408693	1.3289546	0.5355533	-0.010131421
Ti	-2.2466850	0.3006538	0.7189892	-0.095737741
Mn	-0.9471002	1.4906270	-0.4858943	-0.608090822
Fe	-1.7470099	1.2996384	-1.0297289	0.509862485
Ni	-1.8828286	0.8349264	-1.2588754	0.338954347
Rb	-2.2167861	0.4429959	0.8386270	0.606932590
Sr	-0.3809755	0.3749846	2.0384651	1.098812555
Y	-0.6634467	1.4232319	0.9589565	-1.631834719
Cr	-1.9926516	-0.7573885	0.3725702	-1.026751936

Element-color-time PCA: The methodology used for the EO PCA was repeated for the ECT (Element-color-time) PCA. The Kaiser method suggests that the first four PCs are significant, with the results of the test given in Figure 11 (Gortezko and Bühner, 2022). The site and species scores for PCs 1 through 5 were then extracted from the ECT PCA As with the EO PCA, these values were then used to construct a series of site score scatterplots and corresponding biplots. The resulting plots and table of extracted species scores are given in Figures 12 – 14 and Table 2.

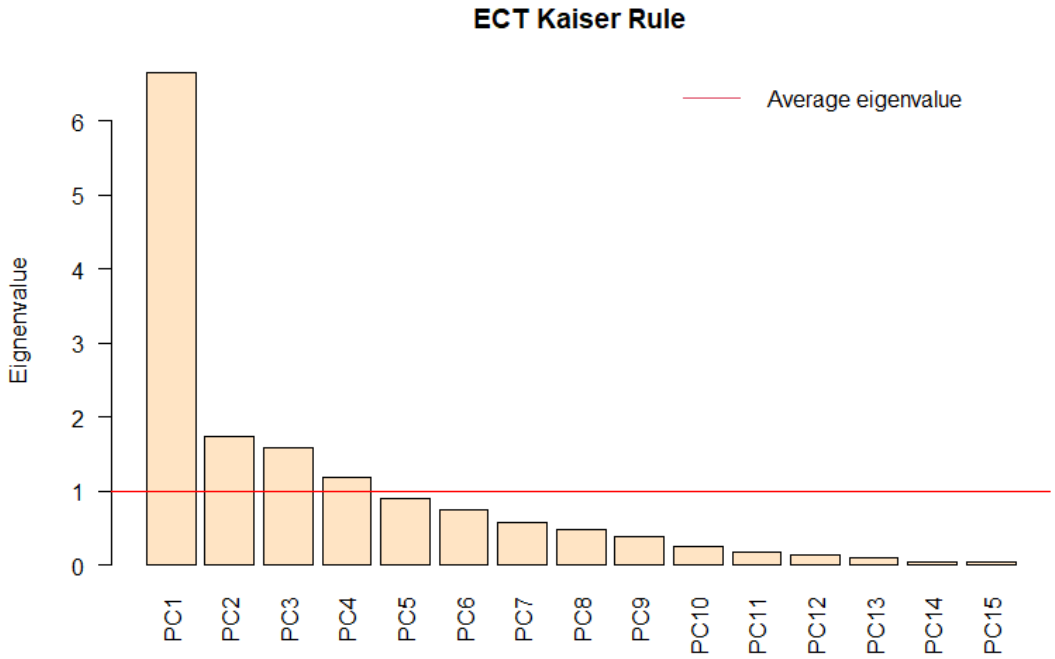

Figure 11: Barplot of results from the Kaiser-rule analysis performed on the ECT PCA. Eigenvalues greater than the average eigenvalue are considered significant. In this case, PCs 1-4 are significant.

The results of the ECT test show similar trends to the results of the EO test. Across the first 5 PCs, time and color show consistent anticorrelation, as demonstrated by the negative covariance in their associated eigenvectors (Figures 12b, 13b, 14b) across all biplots. Gray, low reflectance samples are geologically older than light colored, high reflectance samples. The primary signal on PC1, which is again the most significant axis by a wide margin, was a strong

anti-correlation between Ca (Eigenfunction Score > 1.9) and terrigenous-related elements, including Si, Ti, Al, and K (Eigenfunction score < -1.9). In other words, marls containing terrestrially sourced elements in abundance are anticorrelated with pure carbonates (Van der Weijden 1993). In addition, rock color and geologic age are uncorrelated with Ca content. The primary signal on PC2 is a strong anticorrelation between color (Eigenfunction score ~ -1.5) and time (Eigenfunction score ~ 1.2), as well as a strong correlation between time and Sr (Eigenfunction score ~ 1.4) (Table 2). In the PC2-PC3 biplot (Figure 13), time shows strong positive covariance with Sr, with the eigenvectors of both components aligning closely with a cluster of Outer Shelf sediments. This arrangement resembles the cluster observed in the EO PC2-PC3 biplot (Figure 9).

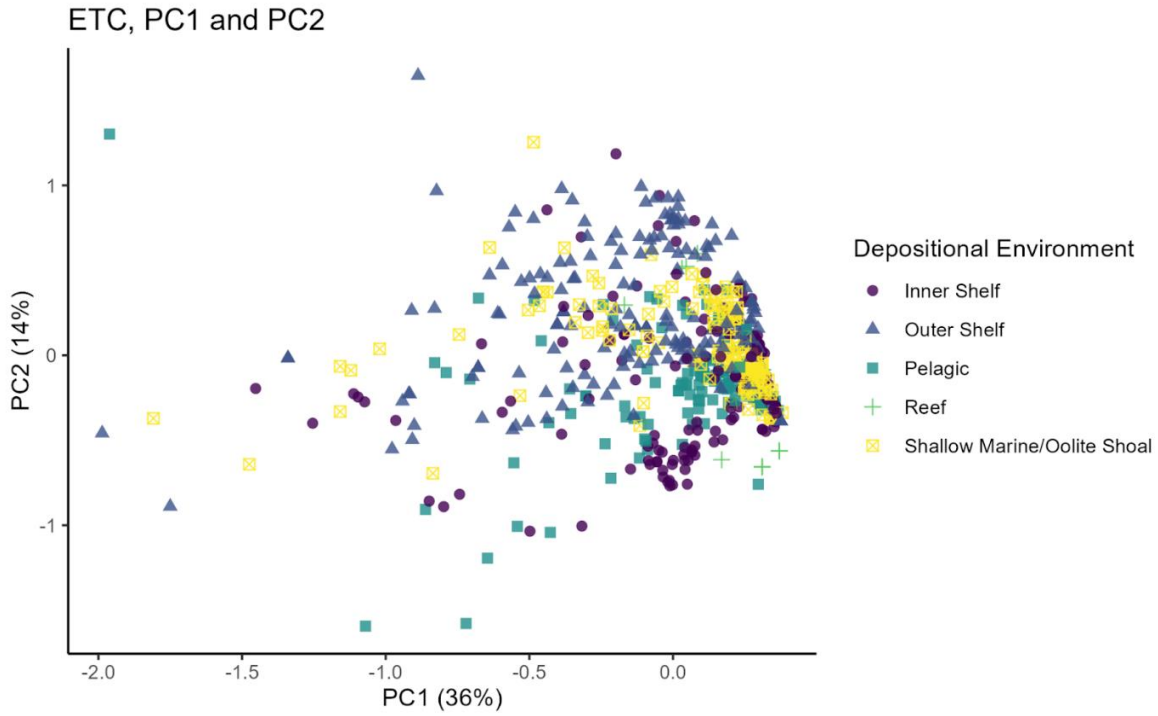

Figure 12a: Biplot of ECT PCA site scores for PC1 and PC2. The percentage of total variation explained by each PC is shown in the axis labels. The depositional environment of each sample is shown in the key on the right.

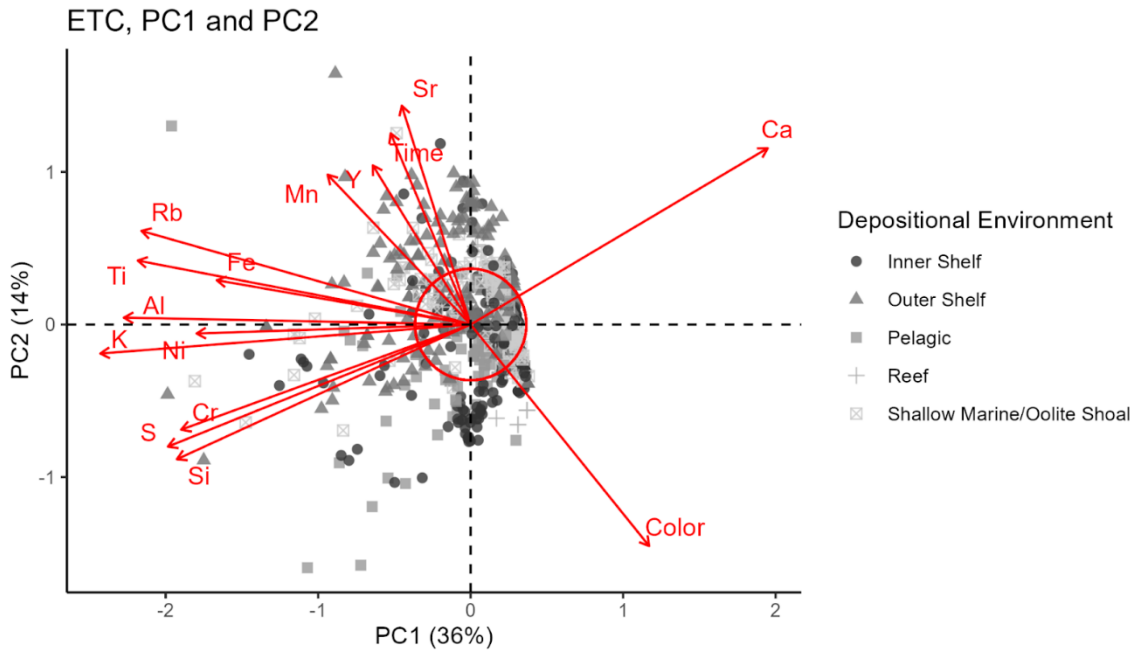

Figure 12b: Biplot of ECT PCA for PC1 and PC2 with eigenvectors plotted in red. Circle of equilibrium is also displayed in red. Note that the vectors for Time and Color are opposite, while the vectors for Ca and several terrigenous-linked elements are orthogonal to both Time and Color.

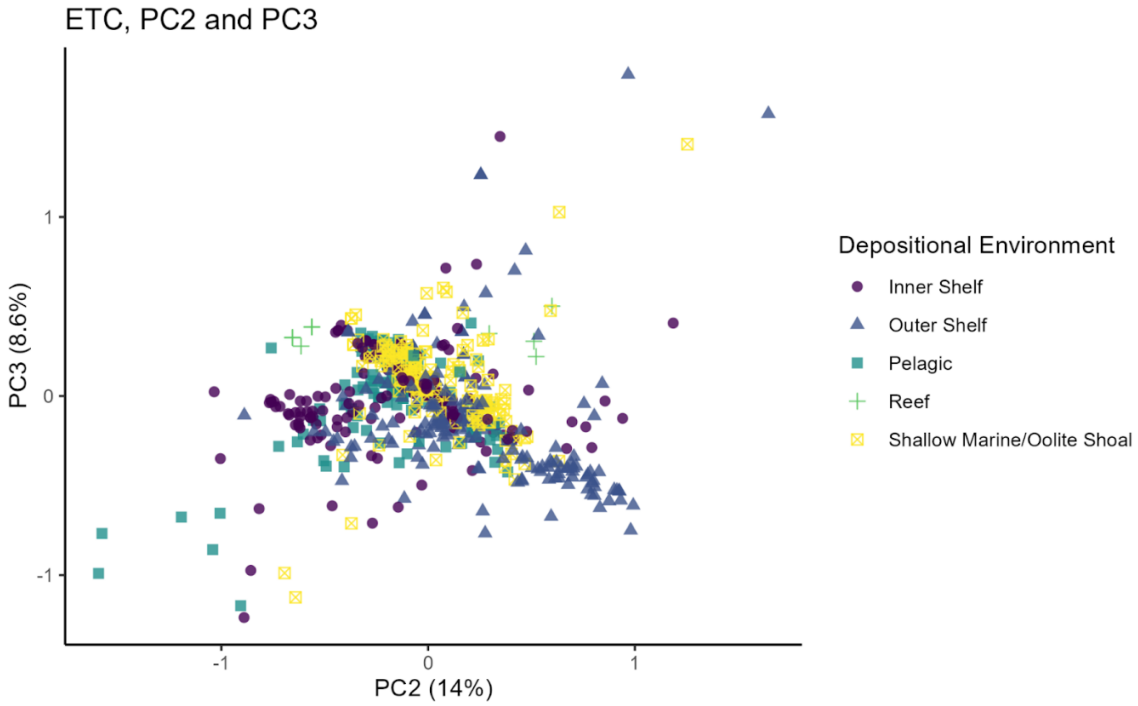

Figure 13a: Biplot of ECT PCA site scores for PC2 and PC3. The percentage of total variation explained by each PC is shown in the axis labels. The depositional environment of each sample is shown in the key on the right.

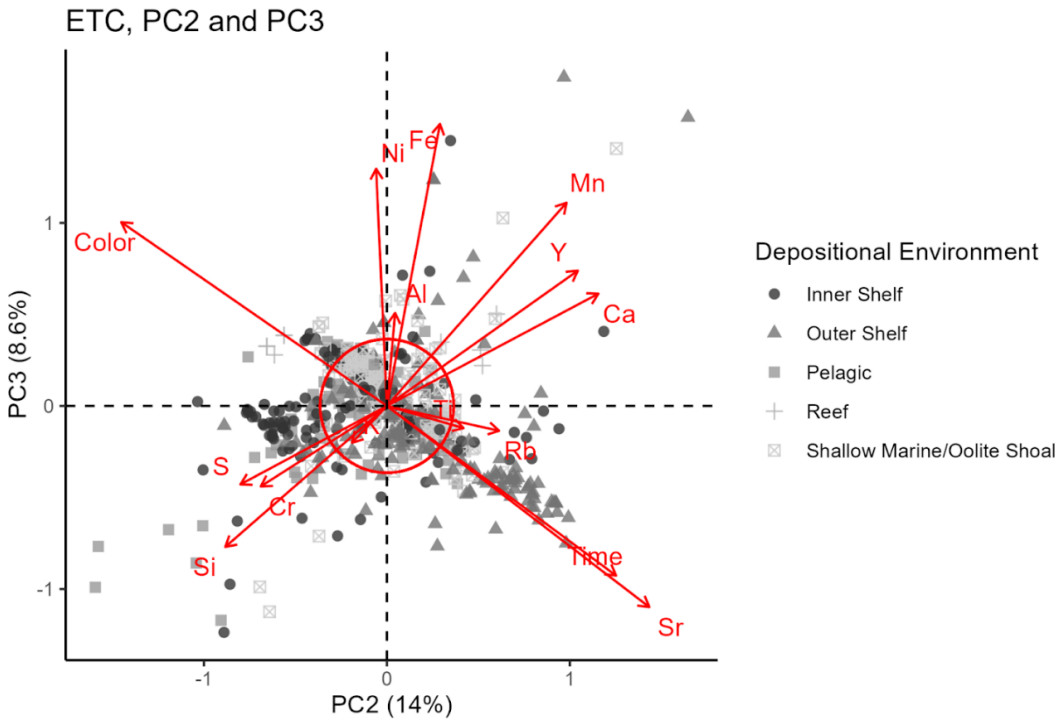

Figure 13b: Biplot of ECT PCA for PC1 and PC2 with eigenvectors plotted in red. Circle of equilibrium is also displayed in red. The most significant feature of this plot is the close correlation between Time and Sr.

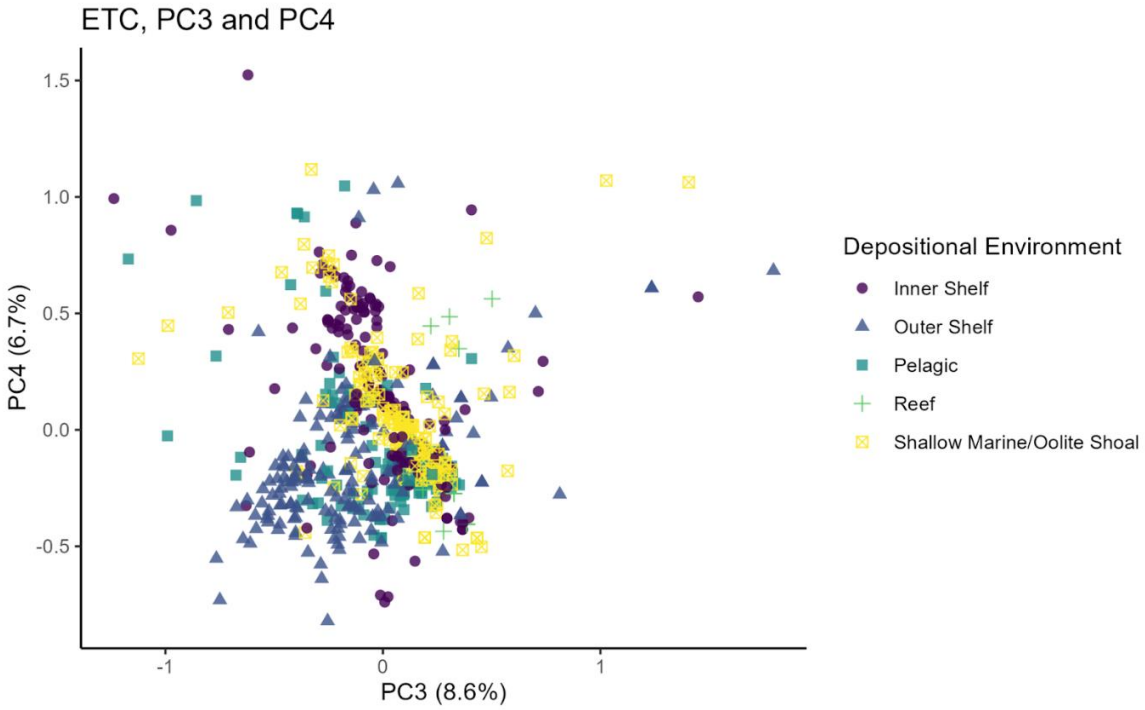

Figure 14a: Biplot of ECT PCA site scores for PC3 and PC4. The percentage of total variation explained by each PC is shown in the axis labels. The depositional environment of each sample is shown in the key on the right.

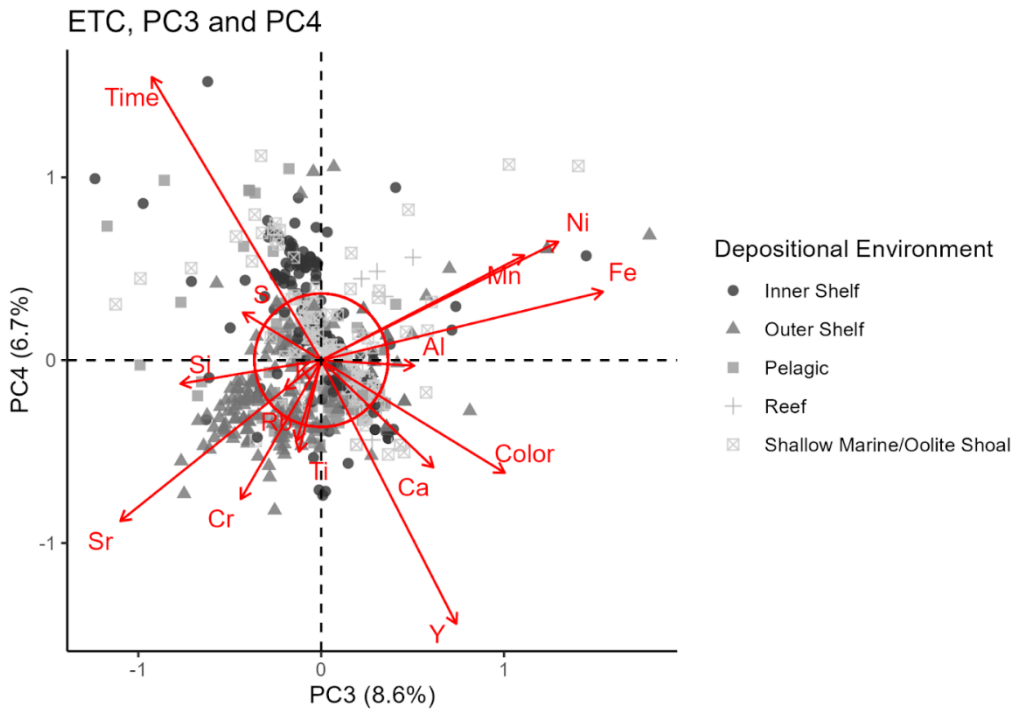

Figure 14b: Biplot of ECT PCA for PC1 and PC2 with eigenvectors plotted in red. Circle of equilibrium is also displayed in red. The eigenvector for Sr appears to correlate closely with a cluster of outer shelf carbonates. The repeated anticorrelation between Time and Color across all significant axes aligns with Sugla's observations of older carbonates being darker than younger carbonates.

It is important to note that Fe is generally poorly correlated with time across each of the PCs (Table 2). The implication of this is that time is not the primary driver of changes in iron content within our sample set. Sugla's original hypothesis was that Paleozoic limestones differ from Mesozoic and younger carbonates are richer in pyrite and other reduced forms of Fe, while younger sediments have more oxidized Fe. Hence, it is likely that the lack of correlation of Fe to time is due to there being multiple oxidation states for Fe; while the overall iron content of the marine carbonates remains relatively consistent across time, the proportion of reduced Fe to oxidized Fe changes (Raiswell and Canfield 1998). However, this hypothesis cannot be tested without information on Fe oxidation states–data that are not obtainable with the Bruker Tracer XRF.

Table 2: ECT PCA eigenfunction scores for each element species, PCs 1 through 5. Values indicate the importance and relative orientation of each element along the axis, with higher magnitude scores indicating that the element is significant to the dimension described by the axis.

Component	PC1	PC2	PC3	PC4	PC5
Color	1.1710414	-1.45179210	1.0038371	-0.61592865	0.00301767
Time	-0.5243335	1.25272358	-0.9267483	1.54887479	0.64096928
Al	-2.2741817	0.04490524	0.5081095	-0.03033865	-0.49853058
Si	-1.9267755	-0.88312038	-0.7699986	-0.12884307	0.50484338
S	-1.9853896	-0.80022913	-0.4282367	0.26081675	0.08928046
K	-2.4290722	-0.19048828	-0.2008590	-0.15971873	-0.15060884
Ca	1.9485183	1.15573212	0.6131990	-0.58617347	-0.11808071
Ti	-2.1829671	0.41898372	-0.1210673	-0.50096263	0.14206341
Mn	-0.9378013	0.98176051	1.1102663	0.57402750	1.07613839
Fe	-1.6649946	0.29025277	1.5405488	0.37472111	-0.70205503
Ni	-1.7974475	-0.05886168	1.2957786	0.64772033	-0.46064406
Rb	-2.1587153	0.61349890	-0.1355434	-0.44309672	-0.50807801
Sr	-0.4516640	1.43415798	-1.0985553	-0.88002014	-1.07064043
Y	-0.6418141	1.04359903	0.7392048	-1.44213315	1.17434877
Cr	-1.8984628	-0.68938720	-0.4394023	-0.75929749	0.68013539

The remaining PCs can be characterized as well, though their low significance in the model begs some degree of skepticism. On PC3, Fe, Mn, and Ni are moderately-well correlated with each other (Eigenfunction scores > 1) and anticorrelated with Sr (Eigenfunction score < -1). On PC4, Time (Eigenfunction score ~ 1.5) is strongly anticorrelated with Yttrium (Y) (Eigenfunction score < -1.4). And on PC5, Y (Eigenfunction score > 1) appears to be anticorrelated with Sr (Eigenfunction score < -1).

RDA Analysis: The results of two RDA analyses performed using this dataset are given below. Due to the structure of the models, which returned only one axis of variation, the results of these analyses are reported as a series of tables rather than biplots.

Table 3: Table of biplot scores for constraining variables from the timeless RDA model after optimization. Note that all biplot scores are negative, indicating anticorrelation with color. Table 3a displays the results of the element-only RDA, while Table 3b displays the results of the time-inclusive RDA.

Element-only RDA (3a)

Element	RDA1
Rb	-0.4148376
Sr	-0.4069546
Ti	-0.3968359
Mn	-0.2057815
Si	-0.2719122
Zn	-0.2577905
Y	-0.1110199
As	-0.2980662

Time-inclusive RDA (3a)

Element	RDA1
Time	-0.4988163
Sr	-0.4069546
Ti	-0.3968359
Ni	-0.2319777
Cr	-0.2555821
Ba	-0.2083791
Zn	-0.2577905
Al	-0.2781826

Color-only RDA: After performing an optimization routine on an all-element RDA that uses only elements as predictors for carbonate color (Figure 17a), the resulting optimized formula included the following elements: Rb, Sr, Ti, Mn, Si, Zn, Y, and As. Notably, Ca is absent from this formula, likely because all limestones are composed dominantly of calcium carbonate. The associated RDA values are given in Table 3a. Rb, Sr, and Ti have the strongest element scores, with all elements in this formula being anti correlated with color. This aligns with the previous observations of terrigenous-sourced elements and Sr being associated with darker marine carbonates. A significance test (Table 4) performed on this RDA shows Rb, Sr, Ti, and Mn as the most likely to be significant, with Rb explaining ~17% of the total variation in sample color. These elements together explain ~31% of the total variation within the sample set (Table 4).

Table 4: Table of results from a significance test performed on the timeless RDA model after optimization. The Table indicates that the Rb, Sr, Ti, and Mn axes are significant (P < 0.001). The significance key is given as follows: 0 = '***', 0.001 = '**', 0.01 = '*', 0.05 = '.', 0.1 = ' '.

Element	Df	Variance	F	Pr > F	Significance Code
Rb	1	0.17209	167.3520	0.001	***
Sr	1	0.07685	74.7340	0.001	***
Ti	1	0.02347	22.8236	0.001	***
Mn	1	0.01317	12.8057	0.001	***
Si	1	0.00913	8.8792	0.003	**
Zn	1	0.00673	6.5427	0.015	*
Y	1	0.00412	4.0043	0.046	*
As	1	0.00548	5.3250	0.020	*
Residual	670	0.68897			

Time and color RDA: Performing a second optimization routine that includes time as a predictor for carbonate color (Table 3b) yields a formula containing the following components: time, Sr, Ti, Ni, Cr, Ba, Zn, Al. As before, Ca is absent from this optimized formula. In this case, time has the greatest variable score, followed by Sr and Ti. Notably, Rb is absent from this version of the formula. Time is the strongest predictor for color and is negatively correlated with rock color. The three components with the strongest eigenvalues after time are Sr, Ti, and Al. A significance test with this RDA (Table 5) suggests that Time, Sr, Ti, and Ni are the components with the highest likelihood of being significant, while Al is the weakest in terms of significance. Time alone in this RDA explains ~25% of the total variation in color, with Sr explaining ~11% of color variation. The total variance explained by these components being ~47% (Table 5).

Table 5: Table of results from a significance test performed on the time-included RDA model after optimization. The Table indicates that the Time, Sr, Ti, and Ni axes are significant (P < 0.001). The significance key is given as follows: 0 = '***', 0.001 = '**', 0.01 = '*', 0.05 = '.', 0.1 = ' '.

Element	Df	Variance	F	Pr > F	Significance Code
Time	1	0.24882	314.3612	0.001	***
Sr	1	0.11955	151.0451	0.001	***
Ti	1	0.06298	79.5694	0.001	***
Ni	1	0.01381	17.4416	0.001	***
Cr	1	0.00980	12.3864	0.002	**
Ba	1	0.00513	6.4752	0.009	**
Zn	1	0.00493	6.2324	0.011	*
Al	1	0.00468	5.9087	0.015	*
Residual	670	0.53031			

DISCUSSION

Geochemistry and Color: To review, if Sugla's hypothesis that changes in the rate of BSR due to marine oxygenation drove the observed changes in carbonate color across the Paleozoic and Mesozoic, the following trends would be expected to appear across each model: positive correlation between Fe and S; higher Fe and S in black and dark gray rocks ; higher Fe and S in older rocks, particularly those from the Paleozoic; and positive correlation between S and sulfide-forming trace elements (Cu, Zn) (Berner 1984; Calvert 1993). One corollary to this hypothesis is the potential for Mn to correlate with Fe and S, as manganese reduction is an intermediate metabolic pathway that, like BSR, also occurs in reducing environment, albeit with weaker efficiency (Burdige 1993).

PCA Analysis: The PCA analyses reveal more about the relative relationships of the various geochemical components to each other, color, and time. The strongest signal in both the EO and ECT PCAs occurs along PC1, which explains 40% of the variation in color for the EO PCA and 36% of the variation in color for the ECT PCA. In both models, PC1 appears to represent the amount of Ca in the sample and ranges from nearly pure pelagic carbonates on the positive end to marls with significant terrigenous components on the negative end. The strongest signals along this principal component are the strong positive Ca eigenvalue (approximately Eigenfunction score = +2) and a series of strong negative eigenvalues for Al, Si, S, K, Fe, Ni, Rb, and Cr (Eigenfunction score = -2 or less). These elements are typically more abundant in marls, which contain a significant quantity of terrigenous-sourced sediments like sand, silt, and clay (Einsele 1982). Therefore, it is likely that PC1 in both PCA analyses represents carbonate purity, with samples with more positive site scores representing pure carbonates and those with more negative scores representing marls.

PC2, meanwhile, appears to represent the axis of color (Eigenfunction score < -1.4) versus time (Eigenfunction score > 1.2), based on the observation that the two components score most significantly on this PC out of any. Furthermore, looking at how the site scores for each of these PCs plot against time (Figures 15a and 15b) reveals more evidence in support of this interpretation. Figure 15a suggests that PC1 has no major temporal component, while Figure 15b shows that PC2 has a strong temporal component. Anticorrelation between time and color is to be expected, as it has been demonstrated that older marine carbonates tend to be darker than younger carbonates (Sugla 2021). Moreover, this relationship remains true across all PC axes and in the RDA analyses, which is a positive signal that older carbonates are indeed consistently darker than younger ones.

These conclusions are further supported by the relationship between color and the element vectors in the biplots for the ECT PCA (Figure 12b). The direction defined by the vectors of Ca and several terrigenous elements (Si, S, K, Cr, and Ti) is orthogonal to the direction defined by the vectors for color and time. When species vectors in a PCA biplot are orthogonal, it indicates a lack of correlation or anticorrelation between these species in the data set. The fact that these two directions are nearly perfectly orthogonal to one another implies that there is no strong relationship between color and carbonate purity or time and carbonate purity, at least in PCs 1 and 2 (Figure 12b). This can be interpreted as indicating that marls are present throughout the entirety of the geologic record, and therefore there is no significant temporal component to the variation in terrigenous-sourced material in marine carbonates over the past 500 Mya. And look again at Figure 15a, there does not appear to be a significant temporal component to the ECT PC1, reinforcing this interpretation.

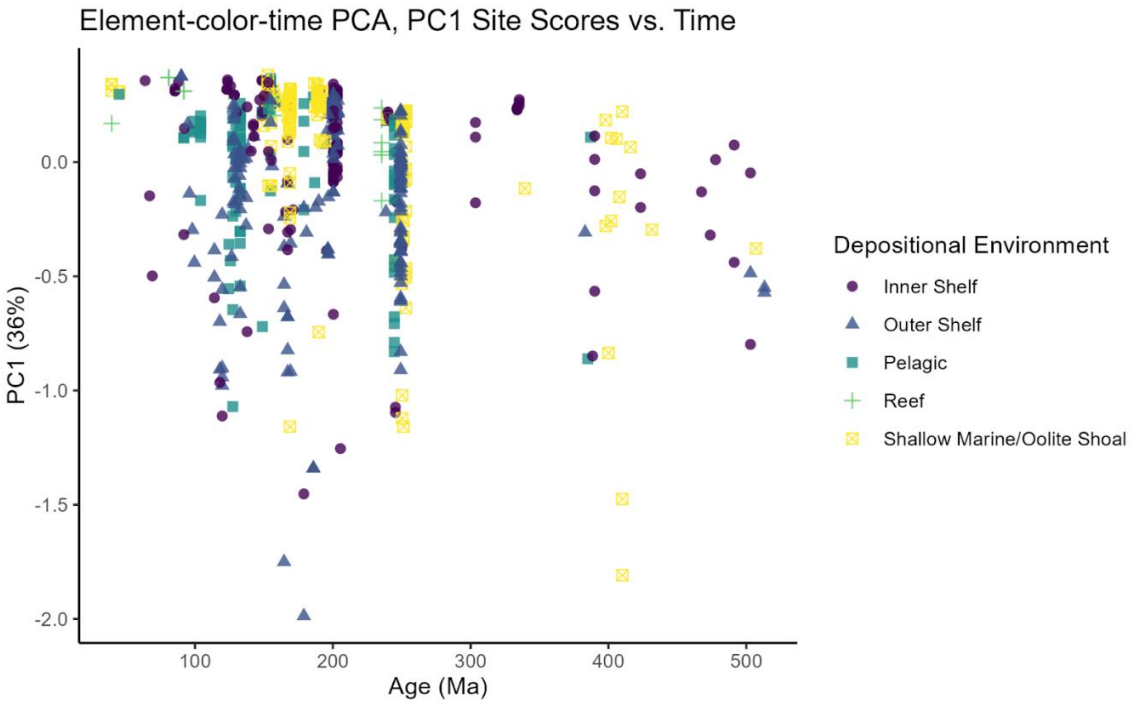

Figure 15a: Plot of sample site scores for the ECT model PC1 versus sample age. Note the lack of a strong temporal trend in the site scores, which indicates this PC represents a non-temporal variation in the dataset.

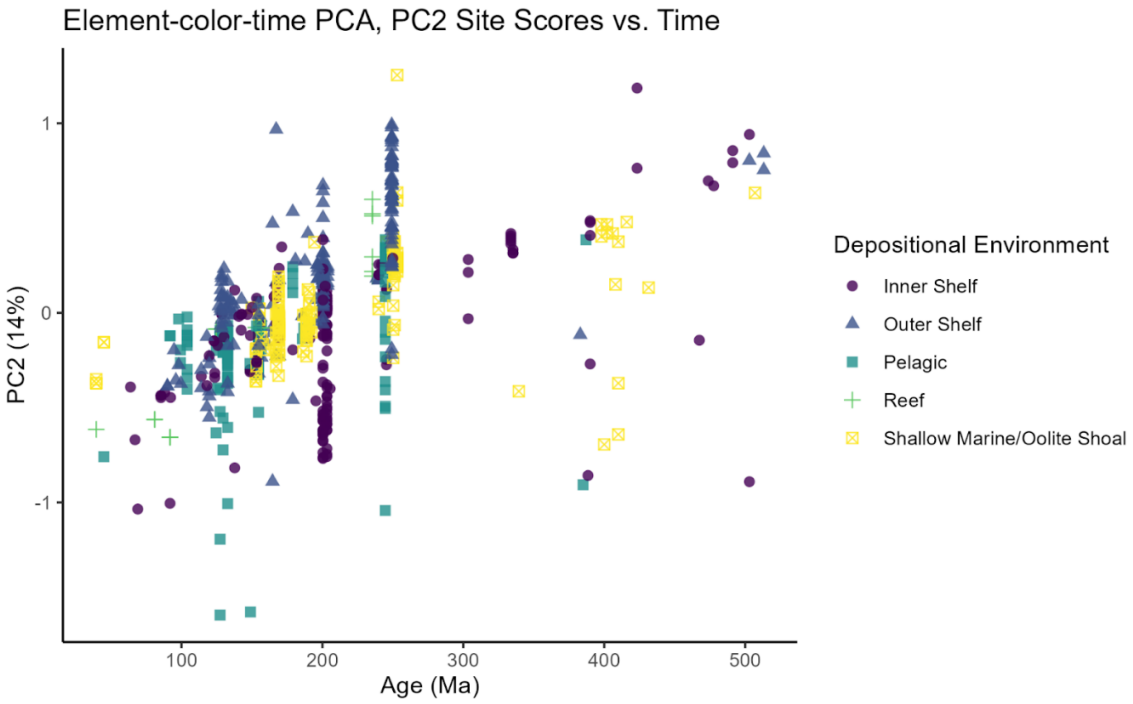

Figure 15b: Plot of sample site scores for the ECT model PC2 versus sample age. The presence of a temporal trend in the site scores supports the conclusion that PC2 represents the color-time variation within the dataset.

Based on the results of the ECT PCA, it appears that there is little to support the hypothesis that BSR is the driving force behind carbonate color. The strongest evidence in favor of Sugla's hypothesis is that S and Ca are anticorrelated on PC1 in the ECT PCA model (Table 2). This suggests that the marls in this data set are more S-rich than the purer carbonates, which aligns with Sugla's expectations that the darker, less-pure carbonates would have more pyrite. However, this is disputed by the observation that the eigenvector of S is orthogonal to the eigenvectors of both color and time in the biplot of PC1 and PC2 (Figure 12b), which are the two most significant axes of variation. The orthogonality of S to the color-time axis goes against two of the primary expectations of Sugla's hypothesis, that sulfur content should correlate with age and anticorrelate with lighter carbonate colors if pyrite is the dominant colorant.

In addition to the lack of any correlation (positive or negative) between S and color or age, there is also no significant correlation between S and Fe in the biplots. While the eigenvectors of the two elements are not orthogonal to one another (Figure 12b), they are also not closely aligned, lying at an angle of approximately 45°. The weak correlation between S and Fe can be explained by the fact that the two elements do not exclusively form pyrite in marine carbonates and can coexist in different mineral phases. Fe has multiple redox states and can form several minerals of varying coloration; while pyrite (FeS_2) is typically very dark in sediment, iron oxides (hematite, goethite, etc.) can range from dark black to reddish brown in color, with reddish-brown sediments returning moderate reflectance at 700 nm (Sugla 2021; Raiswell and Canfield 1998; Myrow 2003). Meanwhile, the geochemistry of S within marine carbonates is highly complex and can be influenced by multiple factors including the rate of organic carbon sedimentation, inorganic carbonate substitution, and the formation of euxinic conditions (Takano 1985). As for the lack of correlation between S and sulfide-forming elements, the majority of

such elements were excluded from the models on the basis that the handheld Bruker Tracer was unable to detect them with the necessary level of consistency (Figures 5d - 5e). Overall, the results of the ECT PCA model do not support the hypothesis that changes in pyrite deposition via BSR drove the overall lightening of marine carbonates from the Paleozoic to the Mesozoic.

RDA Analysis: Moving to the RDA analysis, the results of these seem to align with our previous assessment of the ECT PCA, especially PC1. This is true of both the color-only (Table 3a) and time-inclusive (Table 3b) RDAs, with Ti, Cr, Ni, and Al appearing in the optimized formulas for both and having strongly negative values, indicating anticorrelation with color. The higher reflectance, more oxidized colors are associated with lower abundances of lithogenic elements like Al and Ti. These results imply that marls make up a greater proportion of the black and dark gray carbonates within this data set–an observation consistent with most of the Paleozoic carbonate rocks coming from epicontinental systems proximal to sources of terrigenous sediment (Walker et al. 2002).

One element that stands out in both RDA models is strontium (Sr), which is one of the few trace elements that the XRF Tracer was able to detect consistently across samples (Figure 4a - 4d). Sr places high in significance in the Random Forest model (Figure 6b) as well as in both RDA models (Tables 4 and 5). The PCA models, meanwhile, don't feature Sr as prominently, though it scores highly on several significant PCs; PCs 2, 3 and 4 in the element-only model (Figures 9-10, Table 1), and PCs 2 and 3 in the element-color-time model (Figure 13, Table 2). The fact that Sr doesn't score highly on the first PC in either PCA model immediately brings its importance into question.

Looking more closely at the PCA models, we can see in the biplots shown in Figures 9b, 10b, 13b, and 14b that the eigenvector of Sr repeatedly correlates closely with clusters of outer

shelf carbonates. Extracting these samples from the dataset reveals that the majority originate from the Union Wash formation, located near the Inyo Mountains in California. The samples from this formation are all black to dark gray, indicating that they were deposited under anoxic to euxinic conditions (Woods et al 1999). Several samples from this formation show evidence of diagenetic alteration in the form of recemented fractures (Figure 16). When plotted against time, these samples comprise a significant spike in Sr, as shown in Figure 17. This suggests that the significance placed on Sr by each of the models in this study might be the result of a diagenetic signal from a highly altered set of samples, rather than a depositional signal of any importance to the central question of this study. This conclusion is further supported by the fact that Sr abundances are rarely used in studies of marine carbonates outside of quantifying changes in the ratio of Mg to Ca in seawater (Steuber and Veiser 2002). A full petrographic analysis is needed to identify the nature of the diagenesis that these samples have been subjected to, but the visible features of the samples themselves are enough to argue in favor of this conclusion (Figure 16).

Figure 16 : Picture of two Union Wash samples, UW-12 (left) and UW-29 (right). Both samples show varying degrees of diagenetic alteration, with UW-29 displaying significant fracturing and re-cementation.

One more key observation found in the results of my RDA models is that the residuals for both the timeless and time-inclusive RDAs are very high; the residual for the timeless RDA is ~ 0.69, and the residual for the time-inclusive RDA is ~ 0.53. The implication is that the majority of the variation in color is not explained by the elemental content of the samples, even when considered with the age of the sample. This suggests that the color of the samples is coming from non-mineralogical components, or at least sources that are not reflected in the major element geochemistry of the samples. One such variable could be organic matter (OM) content, which was not included in this study. Organic matter is a possible colorant for gray and brown rocks, since OM tends to be dark brown or black, and is also a necessary reactant for driving pyrite formation in bacterial sulfate reduction (Berner 1984; Westrich 1984).

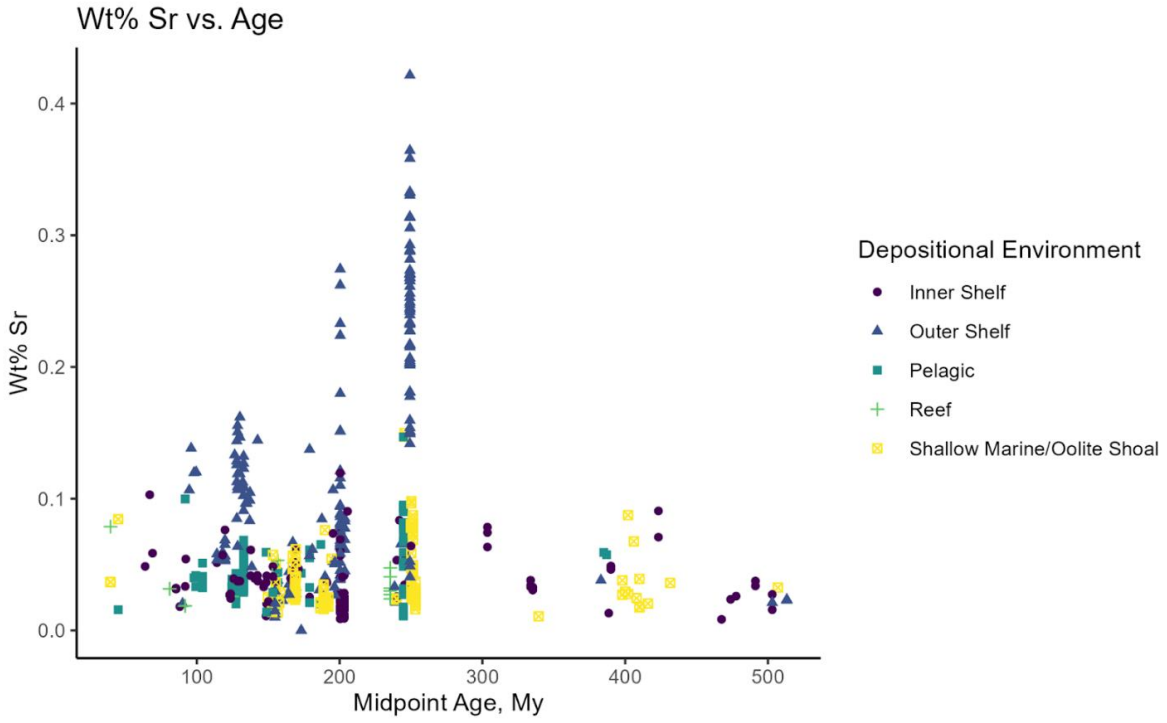

Figure 17: Plot of Wt% Sr versus sample age. Note the spike in Sr concentration in outer shelf samples around 220 Mya. Most of these samples originate from the Union Wash, a deposit located near the Inyo mountains in California.

Assessing the BSR Hypothesis: Considering the results of each analysis, there is little evidence to support the BSR hypothesis based on the element data collected for this study. While S is anticorrelated with Ca, it displays no correlation with the age of the samples nor their color on the most significant PCs (Figure 12) and features only in a modest way in the Random Forest model (Figure 6). Moreover, the correlation between S and Fe is weak at best, and the lack of consistent data for sulfide-forming trace elements precludes any further conclusions.

Overall, the results of each of the models constructed for this study indicate that pyrite is not a major colorant in the samples included within this dataset. If this is indeed the case, organic matter is most likely the dominant colorant in the black and gray carbonates (Myrow 2003). This is a reasonable interpretation based on the facts that Paleozoic samples are typically rich in both preserved OM and pyrite, and the deposition of framboidal pyrite also directly impacts OM preservation (Canfield 1994). Furthermore, multiple interrelated processes exert control on both BSR and OM preservation, including the availability of reactive iron, increasing porewater O_2, and ventilation of marine sediments by active bioturbators, the last of which depletes inventories of both pyrite and OM (Meyers 2007; Canfield 1994; Berner and Westrich 1985). So an increase in marine O_2 during the Mesozoic would have the same impact on carbonate color regardless of whether the primary colorant is pyrite or OM. Seeing as there is already ample evidence for the onset of a marine oxygenation event around 200 Mya in the I/Ca record and bioturbation record, the results of this study point towards OM as the most likely candidate for a major colorant in Paleozoic and dark Mesozoic carbonates (Myrow 2003; Lu et al. 2018; Thayer 1983). This gives direction for future studies following up on the results of Sugla's project.

Limestones, Marls, and Epicontinental Seas: One other feature of the models that warrants further investigation is the relationship between sample age and terrigenous content.

More specifically, why are marls typical of Paleozoic carbonates, while purer carbonates like limestones more typical of the Mesozoic? The Random Forest (Figure 6a) and time-inclusive RDA (Tables 3a and 5) models indicate that there is a strong correlation between sample age and terrigenous elements, with older samples containing a greater proportion of terrigenous-sourced material. Paleozoic samples are primarily represented by marls, which would explain why these terrigenous-linked elements are acting as strong predictors of color in the Random Forest and RDA models. As for the element-color-time PCA model, it is detecting the marl-limestone split independently of age; marls are present throughout the entire study period, and because PCA is able to resolve multiple axes of variation separately, it separates the relationship between terrigenous content and age. But while the results of the models indicate that marls dominate in the Paleozoic, they alone cannot explain the geological processes behind this trend.

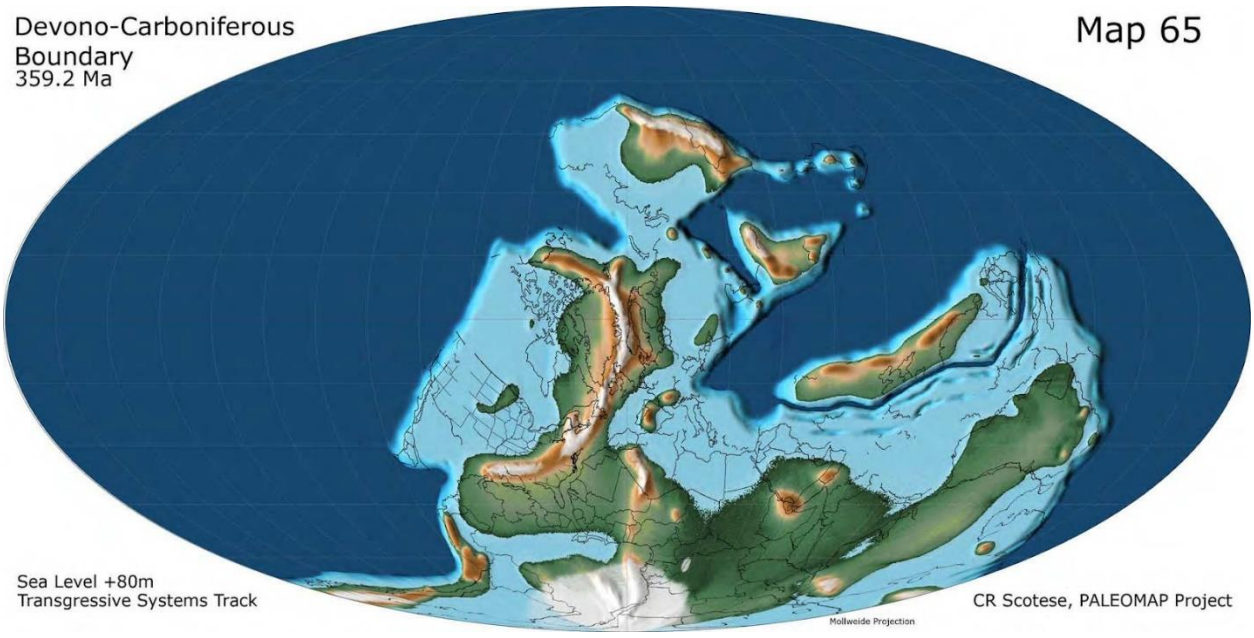

Figure 18: Paleo-reconstruction of Earth tectonic plates during the Devonian-Carboniferous boundary, approximately 360 Mya, produced by CS Scotese as part of the PALEOMAPS project (CS Scotese 2014). Note the extent of shallow, epicontinental seas, which cover significantly more area than in the modern oceans.

Two factors that could explain this shift in carbonate makeup were previously proposed by Sugla in his study of carbonate color: changes in epicontinental sea cover and the evolution of

pelagic calcifiers. The majority of Paleozoic carbonates within this sample set come from epicontinental settings, particularly inner shelf environments, as illustrated by Figure 1. Continental inundation during the Paleozoic was significantly higher than in the Mesozoic or Cenozoic, as demonstrated by the paleogeographic reconstructions produced by CS Scotese in his PALEOMAPS project (Figure 18) (CS Scotese 2021). Epicontinental seas are often areas of high biological productivity, as illustrated by modern epicontinental seas including parts of the Baltic Sea, the Sunda shelf, and the Yellow Sea (Weckström et al. 2017; Sigman and Haim 2012). Their high biological productivity promotes the burial and preservation of organic matter, resulting in sediments that are typically dark brown to black in color (Myrow 2003). Additionally, epicontinental sediments tend to have elevated levels of terrigenous-sourced content owing to their proximity to land (Duff et al. 1967; Jarvis et al. 2001; Hesse and Schacht 2011). Multiple factors account for the increased presence of terrigenous material found in epicontinental marine sediments, including direct inputs from rivers and surface runoff and fluctuations in sea level that regularly exposed the shelf to erosion and progradation of nearshore facies over deeper marine sediments (Duff et al. 1967; Alexander et al. 1991; Jarvis et al 2001; Varejao et al 2021). The combination of increased OM burial and terrigenous material in Paleozoic epicontinental carbonates could partially explain why the Random Forest and RDA models include terrigenous-linked elements as significant predictors of color.

However, the change in the extent of epicontinental seas isn't the only factor relevant to this discussion. Another notable feature of Sugla's results is the near complete absence of pelagic carbonates prior to approximately 250 My (Figure 1). The majority of pelagic carbonates collected by Sugla consist of white and tan carbonate-rich limestones, which only begin to appear in the record during the early to mid-Mesozoic (Sugla 2021). There have been multiple

explanations proposed for the apparent lack of pelagic carbonates in the Paleozoic geologic record, such as the poor preservation of deep-water marine rocks due to tectonic recycling of the seafloor (Mackenzie and Garrels 1971). However, one newer hypothesis is that the abrupt appearance of pelagic carbonates may be related to the evolution of planktonic calcifiers over the Paleozoic and Mesozoic. The authors of Lu et al. (2018) note that large pelagic calcifiers only appear in the fossil record during the mid to late Triassic, around 220 Mya. The lack of pelagic calcifiers prior to the Triassic may help to explain the low abundance of pelagic carbonates during the Paleozoic, as well as why there are fewer limestones and more marls from the Paleozoic. It has even been proposed that the evolution of planktonic calcifiers directly contributed to the onset of widespread marine oxygenation during the early Mesozoic by altering the way oxygen is consumed through the water column, allowing for greater vertical diffusion of O_2 (Lu et al. 2018; Meyer et al. 2016).

Data Uncertainties: The most significant blind spots present within this study are the lack of data on the concentration of organic carbon in our carbonate samples, the lack of redox state data for iron (Fe), the question of how diagenesis may have altered the samples post-formation, and the variable resolution and accuracy of the XRF data between elements. Obtaining measurements of organic carbon content would be a valuable addition, to test the hypothesis that the black and brown marls in the dataset originated from epicontinental seas with high levels of biological productivity and OM burial. Having OM data would also present an opportunity to further test the general hypothesis that carbonate color acts as a proxy for marine oxygenation as presented by Sugla.

Having data on the redox states of iron in each sample would provide another avenue for testing the oxygen hypothesis. One expectation is that Paleozoic carbonates should contain more

reduced forms of iron (e.g. Fe^{2+}), while oxidized Fe (e.g. Fe^{3+}) would become more common after ~220 Mya due to O_2 exposure, either in the water column or after initial deposition via the bioturbation of sediments (Van de Velde and Meysman 2016). Moreover, having a more thorough record of iron redox states would help in addressing the role of framboidal pyrite in determining carbonate color, since iron in pyrite only occurs as Fe^{2+}. As it stands, S shows no clear correlation to Fe or carbonate color in my data set. Characterizing iron according to its redox state could provide more insight into the potential mineralogy of the carbonates included in this study.

The effects of diagenesis on the carbonates included in this set is one that is both important to address and difficult to make broad generalizations about. Studies have shown that diagenetic processes can affect the concentrations of trace elements in carbonates that have been altered, sometimes overprinting the original depositional signal (Hood et al. 2018). However, variability in the timing, intensity, and fluid chemistry between different settings makes it difficult to generalize the impacts of diagenesis on marine carbonate chemistry (Hood et al. 2018). Assessing the specific impacts of diagenesis would likely require at least one petrographic assessment for each of the geologic formations represented in this sample set. Some samples that could benefit from such analysis include the Union Wash samples with their high Sr content, as well as a subset of samples from the Heidelberg collection which display elevated concentrations of Zn. As for the effects of exposure and weathering on the samples, this can be controlled by using only freshly exposed material when analyzing samples using the Bruker XRF tracer (Quye-Sawyer et al. 2015).

Finally, the largest area of improvement for this study is in the resolution of the geochemical data gathered by the XRF Bruker Tracer, as well as the lack of data for multiple

elements. The Burker Tracer was able to accurately estimate the elemental Wt% for most major elements, including Ca, Si, Fe, and Al, but was unable to accurately detect Na or Mg due to the lack of a vacuum (Figures 4a - 4d). This issue can be rectified by placing the chamber under a vacuum using an external pump. Furthermore, the ability to the Bruker Tracer to detect trace elements was somewhat variable, with many elements not being detected at all, and some of those that were detected varying in accuracy across different standards (Figure 4b). This is likely due to the higher detection threshold and lower overall resolution of the handheld Bruker Tracer compared to a traditional XRF.

If the methods of data collection from this study were to be repeated either for the same sample set or another set, one recommendation would be to run the Bruker Tracer in a vacuum. This change should improve both the detection of Na and Mg, while also potentially improving the overall accuracy of the tracer. Another change that could be made to the methodology would be to double the duration of each scan from 30 seconds to 60 seconds, in order to provide more detections and thereby improve the Bruker Tracer's estimations of Wt% content. Increasing the duration of each scan beyond 60 seconds would likely have diminishing returns based on studies using similar handheld XRF hand-held units (Quye-Sawyer et al. 2015). However, it is unlikely that better XRF data alone would significantly shift my conclusions. The handheld Bruker Tracer was able to capture the major element content of the carbonates in a semi-quantitative manner, and the results indicate that differences in major element content is not the driving factor behind the variation in carbonate color over the past 500 My.

CONCLUSION

In conclusion, the geochemical data collected from 679 marine carbonates contradicts Sugla's hypothesis that the observed changes in marine carbonate color over the past 500 Ma due to increasing marine oxygenation were mediated by changes in the rate of BSR. The bulk geochemical data alone does not support the hypothesis that pyrite is the dominant colorant in black and dark gray carbonates, based on the lack of any expected correlation between S, Fe, color, and sample age. This leads to the conclusion that other factors are responsible for driving the transition of marine carbonates from universally black and gray in the Paleozoic to tan and white over the course of the Mesozoic, with organic matter being a likely candidate. Overall, the results of this study provide a guide for further investigation into this topic, pointing out a direction for future studies to follow up on.

This study will also hopefully serve as a foundation for future studies using more precise methods of geochemical analysis and characterization. With the combination of Sugla's data and the geochemical data collected for this study, there now exists a sample set of marine carbonates from throughout the Paleozoic and Mesozoic that have been characterized for their formation, age, depositional environment, color, and estimated element Wt% content for multiple major earth elements and trace elements. These combined data should provide fertile ground for future studies using more precise methods, such as TOC measurements, full XRF spectrometry and ICP analysis. One aspect of the data that warrants further exploration is the elevated strontium content of the Union Wash samples and what it might signify about the geological nature of the locality. The strontium record exemplifies the potential of the data to serve as a foundation for further research into the geochemistry and geology of both the marine carbonates included in this study and marine carbonates in general.

APPENDIX

Table 6: Elemental percentages of the Bruker XRF Tracer comparison test using standard sample ECRM from Mystandards. Standard values taken from: https://www.my-standards.com/media/eb/21/45/1682509010/ECRM752-1-NP_ProductInformationSheet_2023-04-04_V4.0.pdf

Analyte	ECRM	XRF.Scan.1	XRF.Scan.2	XRF.Scan.3
Ca	39.59426	36.9914	36.9981	36.884
Ti	0.00524	0.0047	0.0043	0.006
V	0.000276	0	0	0
Cr	0.00068	0	0	0
Mn	0.00855	0.0111	0.0106	0.0109
Cu	0.000132	0	0	0
Zn	0.000439	0	0	0
Ga	1.96E-05	0	0	0
Rb	4.40E-05	0	0	0
Sr	0.0154	0.0194	0.0191	0.0195
Y	0.000197	0.0016	0.0017	0.0016
Mo	8.00E-06	0.0024	0.0018	0.0024
Ba	0.00547	0	0	0
Pb	0.000151	0.0009	0.0009	0.0009
Th	3.60E-06	0	0	0
U	4.87E-05	0.0024	0.0025	0

Table 7: Elemental percentages of the Bruker XRF Tracer comparison test using standard sample GH-NP from Mystandards. Standard values taken from: https://www.my-standards.com/media/01/fd/70/1682509793/GH-NP_ProductInformationSheet_2023-04-04_V4.0.pdf

Analyte	GH-NP	XRF.Scan.1	XRF.Scan.2	XRF.Scan.3
Na	2.856151	1.4935	1.6644	1.5238
Mg	0.018091	0	0	0
Al	6.615634	4.2833	4.491	5.3529
Si	35.43157	31.1561	31.0306	33.4819

P	0.004364	0	0	0
K	3.951503	2.9005	2.9204	2.9782
Ca	0.493144	0.4021	0.3968	0.4063
Ti	0.047961	0.0381	0.0379	0.0348
Mn	0.038723	0.0325	0.0318	0.0309
Fe	0.93724	0.8345	0.834	0.8326
Cl	0.01	0	0	0
V	5.00E-04	0	0	0
Cr	3.00E-04	0	0	0
Co	3.00E-05	0.0001	0	0
Ni	3.00E-04	0.009	0.0091	0.0092
Cu	3.00E-04	0	0	0
Zn	0.0055	0.0075	0.0074	0.0074
Ga	0.0023	0.0018	0.0018	0.0017
As	4.00E-05	0	0	0
Rb	0.039	0.0318	0.0318	0.032
Sr	0.00087	0.0016	0.0019	0.0019
Y	0.0075	0.0067	0.0069	0.0068
Zr	0.015	0.0127	0.0126	0.0122
Nb	0.0085	0.007	0.007	0.0069
Mo	2.00E-04	0	0	0
Ba	0.002	0	0	0
Pb	0.0045	0.0021	0.0022	0.0022
Th	0.0087	0.0039	0.0039	0.0039
U	0.0018	0.0015	0.0013	0.0014
S	0.007	0.6757	0.6778	0.6737

Table 8: Elemental percentages of the Bruker XRF Tracer comparison test using standard sample SdAR-H1 from Mystandards. Standard values taken from: https://www.my-standards.com/media/06/38/bc/1689592891/SdAR-H1-P_AssignedValues_2023-07-14_V1.0.pdf

Analyte	SdAR-H1	XRF.Scan.1	XRF.Scan.2	XRF.Scan.3
Mg	0.922645	0	0	0
Al	6.261	6.6121	6.5398	6.6843
Si	30.59362	32.3882	32.2857	32.3562
P	0.0807	0.0952	0.0869	0.0882
K	3.4617	4.1203	4.0804	4.102
Ca	1.043459	1.0679	1.0562	1.0585
Ti	0.335631	0.3271	0.324	0.3237
Mn	0.398846	0.4038	0.3987	0.4025
Fe	4.5113	4.6971	4.62	4.6567
V	0.00732	0.0151	0.0133	0.0152
Co	0.00556	0.0029	0.0029	0.003
Ni	0.0234	0.0113	0.0102	0.0108
Cu	0.117	0.1233	0.1206	0.1227
Zn	0.3725	0.3856	0.3781	0.3817
Ga	0.00156	0	0	0
Rb	0.0154	0.0098	0.0096	0.0095
Sr	0.0182	0.0213	0.0206	0.0207
Zr	0.0262	0.0242	0.0234	0.0232
Ba	0.0866	0.0876	0.0981	0.0857
Pb	0.3895	0.1094	0.1095	0.1104
Na	0.8160	0	0	0
Cr	0.0225	0.0223	0.0223	0.0221
Y	0.00254	0.0153	0.0149	0.0155
Nb	0.0022	0	0	0

Mo	0.0066	0.0077	0.0067	0.0076
Th	0.00177	0	0	0
U	0.00042	0	0	0

Table 9: Elemental percentages of the Bruker XRF Tracer comparison test using standard sample SdAR-L2 from Mystandards. Standard values taken from: https://www.my-standards.com/media/45/29/b7/1689592891/SdAR-L2-P_AssignedValues_2023-07-14_V1.0.pdf

Analyte	**SdAR-L2**	**XRF.Scan.1**	**XRF.Scan.2**	**XRF.Scan.3**
Na	1.9733	0	0.1643	0.1365
Al	6.1287	5.27	5.3412	5.374
Si	34.81455	33.3559	33.3375	33.3972
P	0.0349	0.0426	0.043	0.0465
K	3.4036	3.2967	3.3041	3.3234
Ca	0.75758	0.6646	0.6686	0.671
Ti	0.371592	0.2835	0.2871	0.2886
Mn	0.076671	0.0667	0.0666	0.0672
Fe	2.5459	2.1413	2.1504	2.1588
V	0.0035	0.0034	0.005	0.0042
Cr	0.0026	0.0052	0.006	0.0068
Co	0.00054	0.0012	0.0011	0.0012
Ni	0.00143	0.0052	0.0054	0.0054
Cu	0.00508	0.0066	0.0075	0.0069
Zn	0.0201	0.0218	0.0219	0.0213
Rb	0.012	0.0118	0.0118	0.0119
Sr	0.015	0.0181	0.0181	0.0182
Y	0.00555	0.0054	0.0059	0.006
Zr	0.0626	0.0591	0.0583	0.0599
Mo	0.00037	0	0	0

Pb	0.0183	0.0033	0.0032	0.0032
Th	0.0022	0	0	0
U	0.000334	0	0	0
Mg	0.259305	0	0	0
Ga	0.00175	0.0022	0.0022	0.0022
As	0.0017	0.0064	0.0061	0.0062
Nb	0.0063	0.0064	0.0068	0.0065
Ba	0.0812	0.0733	0.0715	0.0723

REFERENCES

1. Ager, Derek Victor (1973). The nature of the stratigraphical record. Macmillan & Halsted Press, N.Y.

2. Alexander, C. R., DeMaster, D. J., & Nittrouer, C. A. (1991). Sediment accumulation in a modern epicontinental-shelf setting: the Yellow Sea. Marine Geology, 98(1), 51-72.

3. Berner, R. A., & Westrich, J. T. (1985) Bioturbation and the early diagenesis of carbon and sulfur. American Journal of Science, 285(3), 193-206.

4. Berner, R. A. (1984). Sedimentary pyrite formation: an update. Geochimica et cosmochimica Acta, 48(4), 605-615.

5. Berner, R. A., & Raiswell, R. (1983). Burial of organic carbon and pyrite sulfur in sediments over Phanerozoic time: a new theory. Geochimica et Cosmochimica Acta, 47(5), 855-862.

6. Breiman, L. (2001). Random Forests. Machine learning, 45, 5-32.

7. Burdige, D. J. (1993). The biogeochemistry of manganese and iron reduction in marine sediments. Earth-Science Reviews, 35(3), 249-284.

8. Calvert, S. E., & Pedersen, T. F. (1993). Geochemistry of recent oxic and anoxic marine sediments: implications for the geological record. Marine geology, 113(1-2), 67-88.

9. Canfield, D. E. (1994) Factors influencing organic carbon preservation in marine sediments. Chemical Geology, 114(3-4), 315-329.

10. Dahl, T. W., Hammarlund, E. U., Anbar, A. D., Bond, D.P., Gill, B. C., Gordon, G. W., Knoll, A. H., Nielsen, A. T., Schovsbo, N. H., Canfield, D. E. (2010) Devonian rise in atmospheric oxygen correlated to the radiations of terrestrial plants and large predatory fish. Proceedings of the National Academy of Sciences USA, 107(42), 17911–17915.

11. Duff, P. M. D., Hallam, A., & Walton, E. K. (1967). Developments in Sedimentology: Cyclic Sedimentation. Elsevier Publishing Company.

12. Einsele, G. (1982). Limestone-marl cycles (periodites): diagnosis, significance, causes—a review. Cyclic and Event Stratification, 8-53.

13. Goretzko, D., & Bühner, M. (2022). Factor retention using machine learning with ordinal data. Applied Psychological Measurement, 46(5), 406-421.

14. Hesse, R., & Schacht, U. (2011). Early diagenesis of deep-sea sediments. Developments in Sedimentology, 63, 557-713.

15. Hood, A. V. S., Planavsky, N. J., Wallace, M. W., & Wang, X. (2018). The effects of diagenesis on geochemical paleoredox proxies in sedimentary carbonates. Geochimica et Cosmochimica Acta, 232, 265-287.

16. Jarvis, I. A. N., Murphy, A. M., & Gale, A. S. (2001). Geochemistry of pelagic and hemipelagic carbonates: criteria for identifying systems tracts and sea-level change. Journal of the Geological Society, 158(4), 685-696.

17. Lu, W., Ridgwell, A., Thomas, E., Hardisty, D. S., Luo, G., Algeo, T. J., Saltzman, M. R., Gill, B. C., Shen, Y., Ling, H. F. and Edwards, C. T. (2018) Late inception of a resiliently oxygenated upper ocean. Science (80-):eaar5372.

18. Mackenzie, F. T., & Garrels, R. M. (1971). Evolution of sedimentary rocks. New York: Norton.

19. Meyer, K. M., Ridgwell, A., & Payne, J. L. (2016). The influence of the biological pump on ocean chemistry: implications for long-term trends in marine redox chemistry, the global carbon cycle, and marine animal ecosystems. Geobiology, 14(3), 207-219.

20. Meyers, S. R. (2007). Production and preservation of organic matter: The significance of iron. Paleoceanography, 22(4).

21. Myrow, P. (2003) Colors of sedimentary rocks. Sedimentology (Springer Netherlands, Dordrecht), pp 251-253.

22. Quye-Sawyer, J., Vandeginste, V., & Johnston, K. J. (2015). Application of handheld energy-dispersive X-ray fluorescence spectrometry to carbonate studies: opportunities and challenges. Journal of Analytical Atomic Spectrometry, 30(7), 1490-1499.

23. Raiswell, R., & Canfield, D. E. (1998). Sources of iron for pyrite formation in marine sediments. American Journal of Science, 298(3), 219-245.

24. Scotese, C. R. (2014). Atlas of Devonian paleogeographic maps, PALEOMAP atlas for ArcGIS, volume 4, the Late Paleozoic, maps 65-72. Mollweide Projection, PALEOMAP Project, Evanston, IL.

25. Scotese, C. R. (2021). An atlas of Phanerozoic paleogeographic maps: the seas come in and the seas go out. Annual Review of Earth and Planetary Sciences, 49, 679-728.

26. Sigman, D. M., & Hain, M. P. (2012). The biological productivity of the ocean. Nature Education Knowledge, 3(10), 21.

27. Steuber, T., & Veizer, J. (2002). Phanerozoic record of plate tectonic control of seawater chemistry and carbonate sedimentation. Geology, 30(12), 1123-1126.

28. Sugla, R. K. (2021). Rising oxygen concentrations as a driver of macroevolutionary trends in marine communities. UC San Diego. ProQuest ID: Sugla_ucsd_0033D_20223. Merritt ID: ark:/13030/m5m96b1x. Retrieved from https://escholarship.org/uc/item/8d0017w4

29. Takano, B. (1985). Geochemical implications of sulfate in sedimentary carbonates. Chemical Geology, 49(4), 393-403.

30. Thayer, C. W. (1983). Sediment-mediated biological disturbance and the evolution of marine benthos. In Biotic interactions in recent and fossil benthic communities (pp. 479-625). Boston, MA: Springer US.

31. Van De Velde, S., & Meysman, F. J. (2016). The influence of bioturbation on iron and sulphur cycling in marine sediments: a model analysis. Aquatic Geochemistry, 22, 469-504.

32. Van der Weijden, C. H. (1993). Geochemical signatures preserved in sediments of the Semaforo and Vrica sections (Calabria, Italy) and their relations with variations of the sedimentary regime. Palaeogeography, palaeoclimatology, palaeoecology, 103(3-4), 203-221.

33. Varejao, F. G., Warren, L. V., Simoes, M. G., Buatois, L. A., Mangano, M. G., Bahniuk Rumbelsperger, A. M., & Assine, M. L. (2021). Mixed siliciclastic–carbonate sedimentation in an evolving epicontinental sea: Aptian record of marginal marine settings in the interior basins of north-eastern Brazil. Sedimentology, 68(5), 2125-2164.

34. Walker, L. J., Wilkinson, B. H., & Ivany, L. C. (2002). Continental drift and Phanerozoic carbonate accumulation in shallow-shelf and deep-marine settings. The Journal of Geology, 110(1), 75-87.

35. Weckström, K., Lewis, J. P., Andrén, E., Ellegaard, M., Rasmussen, P., Ryves, D. B., & Telford, R. (2017). Palaeoenvironmental history of the Baltic Sea: one of the largest Brackish-water ecosystems in the world. Applications of paleoenvironmental techniques in estuarine studies, 615-662.

36. Westrich, J. T., & Berner, R. A. (1984). The role of sedimentary organic matter in bacterial sulfate reduction: The G model tested 1. Limnology and oceanography, 29(2), 236-249.

37. Woods, A. D., Bottjer, D. J., Mutti, M., & Morrison, J. (1999). Lower Triassic large sea-floor carbonate cements: their origin and a mechanism for the prolonged biotic recovery from the end-Permian mass extinction. Geology, 27(7), 645-648.